Title

In vivo bioluminescence imaging of labile iron in xenograft models and liver using FeAL-1, an iron-activatable form of D-luciferin.

Journal

Cell chemical biology, 30(11)

Authors

Gonciarz, Ryan
Jiang, Honglin
Tram, Linh
et al.

Publication Date

2023-11-16

DOI

10.1016/j.chembiol.2023.09.006

Peer reviewed

HHS Public Access

Author manuscript

Cell Chem Biol. Author manuscript; available in PMC 2024 November 16.

Published in final edited form as:

Cell Chem Biol. 2023 November 16; 30(11): 1468–1477.e6. doi:10.1016/j.chembiol.2023.09.006.

In vivo bioluminescence imaging of labile iron in xenograft models and liver using FeAL-1, an iron-activatable form of D-luciferin

Ryan L. Gonciarz[1], **Honglin Jiang**[2], **Linh Tram**[1], **Cedric L. Hugelshofer**[3], **Oscar Ekpenyong**[4], **Ian Knemeyer**[4], **Allegra T. Aron**[5], **Christopher J. Chang**[6], **John A. Flygare**[3], **Eric A. Collisson**[2], **Adam R. Renslo**[1,2,7,*]

[1]Department of Pharmaceutical Chemistry, University of California, San Francisco, San Francisco, California 94158, USA

[2]Helen Diller Family Comprehensive Cancer Center, University of California, San Francisco, San Francisco, California 94158, USA

[3]Department of Discovery Chemistry, Merck & Co., Inc., South San Francisco, California 94080, USA

[4]ADME & Discovery Toxicology, Merck & Co., Inc., South San Francisco, California 94080, USA

[5]Department of Chemistry and Biochemistry, University of Denver, Denver, Colorado, 80208, USA.

[6]Departments of Chemistry and Molecular and Cell Biology, University of California, Berkeley, Berkeley, California, 94720, USA.

[7]Lead contact.

Summary

Dysregulated iron homeostasis underlies diverse pathologies, from ischemia-reperfusion injury to epithelial–mesenchymal transition and drug-tolerant “persister” cancer cell states. Here, we introduce Ferrous Iron Activatable Luciferin-1 (FeAL-1), a small molecule probe for bioluminescent imaging of the labile iron pool (LIP) in luciferase-expressing cells and animals. We find that FeAL-1 detects LIP fluctuations in cells after iron supplementation, depletion, or treatment with hepcidin, the master regulator of systemic iron in mammalian physiology. Utilizing FeAL-1 and a dual-luciferase reporter system, we quantify LIP in mouse liver and three different

*Corresponding Author: Adam R. Renslo adam.renslo@ucsf.edu.

Author contributions: RLG, HJ, CLH, JAF, EAC, and ARR conceived and designed experiments. RLG, LT, HJ, OE, and IK performed experiments. ATA and CJC provided a sample of ICL-1. All authors analyzed data and reviewed the manuscript. JAF, EAC, and ARR supervised research and provided funding

Declaration of interests: EAC and ARR are co-founders and consultants to Tatara Therapeutics.

Supplemental Information

Supplemental information can be found online at

orthotopic pancreatic ductal adenocarcinoma tumors. We observed up to ten-fold increase in FeAL-1 bioluminescent signal in xenograft tumors as compared to healthy liver, the major organ of iron storage in mammals. Treating mice with hepcidin further elevated hepatic LIP, as predicted. These studies reveal a therapeutic index between tumoral and hepatic LIP and suggest an approach to sensitize tumors toward LIP-activated therapeutics.

eTOC Blurb

Gonciarz et. al. describes the small molecule FeAL-1 (iron(Fe)-Activatable Luciferin-1) for the selective detection of labile iron pools (LIP) in cells and animals using standard bioluminescent imaging methods. Using FeAL-1, the researchers find that LIP in mouse xenograft models can substantially exceed that of liver

Introduction

Iron-dependent cofactors empower a diverse range of biochemical reactions and enzyme functions in physiology, including DNA synthesis and repair, mitochondrial respiration, and the transport and storage of oxygen[1,2]. The utility of iron in these processes lies in the ability to cycle between the ferrous (Fe^{2+}) and ferric (Fe^{3+}) states under physiological conditions. Iron homeostasis at the cellular level relies on a highly regulated system of iron import, storage, and export, with the insoluble ferric ion tightly bound to protein chaperones during transport (e.g. transferrin-bound) and storage (e.g. ferritin-bound). Ferrous iron, by contrast, is weakly chelated and water-soluble, comprising the cellular “currency” of iron known as the labile iron pool (LIP). Systemically, iron distribution and storage is regulated by ferroportin, the only known exporter of iron, and its negative regulator hepatic hepcidin[3,4].

Dysregulation of iron homeostasis and “iron addiction” has been described in diverse cancer types and also in drug-tolerant “persister” cancer cells[5–8]. These observations are intriguing, since elevated LIP promotes Fenton-type reactivity and the production of reactive oxygen species (ROS) that are generally toxic to cells[9]. Iron-promoted peroxidation of polyunsaturated fatty acids for example contributes to a non-apoptotic, iron-dependent form of cell death known as ferroptosis[10,11]. To the extent tumors persist or even thrive on a knife’s edge of oxidative stress, the induction of ferroptosis represents a promising new therapeutic strategy in cancer[12,13]. Conversely, the inhibition of ferroptosis is therapeutically desirable in the context of neurodegenerative disease[14], ischemic organ injury[10,15] and cardiomyopathy[16]. Although a variety of small molecules that either induce or inhibit ferroptosis are known, small molecule probes to study or modulate LIP itself have been lacking, particularly for *in vivo* studies.

The Fe^{2+} ion forms weak coordination complexes when compared to the other biologically relevant divalent metal ions in the Irving-Williams series[17]. As a result, activity-based sensing[18] has emerged as a promising modality for detecting ferrous iron selectively in biological settings. In 2013, Chang introduced a biomimetic scaffold that mimics non-heme iron oxidation chemistry for LIP detection[19]. The ability of Fe^{2+} to promote N–O bond *reduction* has been exploited by Hirayama in various turn-on probes based on rhodamine *N*-oxides, as recently reviewed[20], and also in FeP, a probe for two photon imaging[21].

In 2014, we described O–O bond reduction in a 1,2,4-trioxolane scaffold (TRX) as a new modality for LIP detection[22]. We later demonstrated Fe^{2+}-promoted activation of a puromycin reporter for imaging LIP in fixed cells[23] and Chang employed a TRX trigger for FRET-based fluorescence LIP detection[24]. Subsequently, Chang and Renslo introduced ICL-1 (Figure 1), a TRX conjugate of D-aminoluciferin, and the first probe useful for *in vivo* bioluminescence imaging of LIP[25]. Most recently, Renslo and Evans introduced the radioligand ^{18}F-TRX for positron emission tomography (PET) studies of LIP across diverse xenograft models[26,27]. While notable for its translational potential, PET imaging with ^{18}F-TRX requires access to a cyclotron, radiochemistry facilities, and PET imagers.

For most basic science researchers, the utility of bioluminescent imaging (BLI) with D-luciferin remains unrivaled in its broad utility, as has been reviewed[28–30]. The power of this approach is magnified when combined with “caged” forms of D-luciferin that are responsive to specific analytes or enzymatic activities[31–35]. To date, only ICL-1[25] and FP-1[36] have been described for *in vivo* BLI of labile iron, and only (so far) in systemic infection models. Here, we introduce FeAL-1 (Ferrous iron-Activatable Luciferin-1), a second-generation *in vivo* LIP probe based on the more emissive and widely used luciferase substrate D-luciferin. We present a practical synthesis of FeAL-1 and demonstrate its metal ion and oxidation state selectivity for Fe^{2+}. Compared to ICL-1, FeAL-1 exhibits greater sensitivity, particularly after the initial ‘burst’ phase of luminescence, advantages that are consistent with the known behavior of D-aminoluciferins vs. D-luciferin[37]. We describe here optimized protocols for the use of FeAL-1 in cells and mice, and report the use of FeAL-1 to compare LIP levels in the livers of healthy mice with that in the tumors of three orthotopic pancreatic ductal adenocarcinoma (PDA) xenograft models. To our knowledge, this represents the first direct, semi-quantitative comparison of LIP in livers and tumors of live animals, and reveals a therapeutic index for targeting tumors with LIP interacting therapeutics.

Results

Design, Synthesis and Reactivity of FeAL-1.

First-generation luciferin probe ICL-1[25] was based on a D-*amino*luciferin reporter that yields an *in vivo* stable carbamate bond between the TRX moiety and reporter (Figure 1). With FeAL-1, we sought to employ the more emissive D-luciferin as the reporter, but recognized direct conjugation at the phenol function in this substrate would yield a labile carbonate prone to proteolysis *in vivo*. To overcome this issue, we employed a (*N,N’*-dimethyl)ethylenediamine linker used previously[38–43] to cage and release phenolic reporters through a self-immolative cyclization mechanism[44–46]. Accordingly, FeAL-1 was prepared by reaction of enantiopure trioxolane **1** with *N*-Boc (*N,N’*-dimethyl)-ethylenediamine to afford the carbamate intermediate **2** in excellent yields (Figure 2A). Careful deprotection of **2** using acetyl chloride in methanol then afforded **3** as a hydrochloride salt, which was stored as such to avoid premature cyclization of the terminal amine onto the proximal carbamate. Next, 2-cyano-6-hydroxybenzothiazole (**4**) was activated as the corresponding *para*-nitrophenylcarbonate **5** and treated *in situ* with **3**•HCl to produce di-carbamate **6** in acceptable yields (37–52% over two-steps). Installation of the thiazoline ring was achieved by reaction with D-cysteine to afford FeAL-1 (**7**), which proved stable over several months,

when stored as a powder at −20 °C under argon (Figure S1). We next explored the fragmentation of FeAL-1 in reaction with ferrous heme prepared as described[47] but using a solvent mixture of Tris-HCl and DMSO (9:1) to maintain neutral pH during the reaction. As expected, FeAL-1 reacted to afford intermediates **int 1** and **int 2**, followed by release of free D-luciferin as detected by UPLC/MS analysis (Figure 2B and S1). Control experiments confirmed that FeAL-1 was stable in assay media lacking hemin (Figure S1).

FeAL-1 is Selectively Activated by Ferrous Iron.

To assess the ferrous iron selective reactivity of FeAL-1 we incubated FeAL-1 with various s-block and d-block metal ions for 2 hours, followed by the addition of 10 μg/mL luciferase (Figure 3A). Consistent with similar studies of ICL-1 and other TRX-based probes, we observed a robust luminescence response from FeAL-1 when incubated with Fe^{2+} as ferrous ammonium sulfate (FAS) but not with ferric iron (Fe^{3+}) or the other metals ion salts (Figure 3A). Control experiments confirmed that the luminescent response of D-luciferin itself is not affected by increasing concentrations of Fe^{2+}, nor is it significantly altered in the presence of other metal ions (Figure S2). The response of FeAL-1 was also selective for ferrous iron (as FAS) over common cellular reductants, oxidants, and the iron binding protein transferrin in either the apo or iron-bound state, (Figure 3B). Taken together, these data demonstrate that the bioluminescent response of FeAL-1 derives from selective reaction with Fe^{2+} and the coupled release of D-luciferin.

We compared the response of FeAL-1 to ICL-1 under cell free conditions to determine whether the reported[37] differences in response between D-luciferin and D-aminoluciferin were manifest in the context of the two probes. Following a 90-minute incubation of either probe with 1–100 μM FAS, with or without iron chelator 2,2-bipyridine (BPY), we added 100 μg/mL luciferase and imaged the solutions 1 minute and 6 minutes later. Both probes showed a response that was proportional to the concentration of FAS or BPY in the pre-treatment condition (Figure 3C). The luminescent response of both probes was higher at 1 minute, consistent with the initial burst phase of luminescence. However, FeAL-1 bearing D-luciferin showed a much stronger response than ICL-1 at both timepoints, and particularly at the 6-minute timepoint (Figure 3D). These results reflect the higher intrinsic luminescence of D-luciferin and reduced product inhibition as compared to D-aminoluciferin. Analogous cell-free experiments employing nM concentrations of FAS pre-treatment showed that FeAL-1 exhibits a concentration-dependent response well into the nM range, and was again much more sensitive than ICL-1 at the 6-minute timepoint (Figure S2).

FeAL-1 Detects Altered LIP in Cancer Cells.

Having established the sensitivity and selectivity of FeAL-1 for Fe^{2+}, we next asked whether FeAL-1 could detect changing Fe^{2+} levels in luciferase-expressing cancer cell lines. To rule out the possibility of *extracellular* activation of FeAL-1 we used ferric ammonium citrate (FAC, a source of Fe^{3+}) for cellular pre-conditioning, since FeAL-1 was unreactive with FAC (Figure 3A, B) but would still be subject to cellular uptake and reduction to Fe^{2+} by canonical iron acquisition machinery[5,48]. We employed a panel of six luciferase-expressing pancreatic ductal adenocarcinoma (PDA) and colon cancer cell lines, including HCT116-luc, MiaPaCa-2-luc, SW1990-luc, SW620-luc, FC1245-luc, and Colo357-luc for these studies.

First, we compared the cellular responses of FeAL-1 and ICL-1 in MiaPaca2-luc and SW-1990-luc cell lines preconditioned with increasing concentrations of FAC prior to addition of FeAL-1 or ICL-1. Thus, cells were first incubated with or without FAC for 2 hours prior to addition of probe and then imaged after an additional 15 min incubation period to allow for activation. As in the cell-free experiments, we observed a stronger iron-dependent luminescent response from FeAL-1 than from ICL-1 in both cell lines (Figure 4). Across a larger panel of cell lines, we observed a similarly robust bioluminescent signal from FeAL-1 in response to FAC supplementation, as well as the expected reduction in bioluminescence response with BPY iron chelator treatment, with or without FAC (Figure S3). Control experiments confirmed that iron conditioning or chelation did not significantly affect the bioluminescent response of cells treated with D-luciferin instead of FeAL-1 (Figure S4).

Next, we investigated whether FeAL-1 could detect changes to cellular labile iron load in response to the hepatic peptide hormone hepcidin, the negative regulator of the iron export protein ferroportin[49]. Luciferase-expressing PDA and colon cancer cell lines were pre-treated for 16 hours with various concentrations (1, 2 and 4 μg/mL) of hepcidin, either alone or with FAC supplementation or BPY iron chelation. We found that treatment with increasing concentrations of hepcidin led to a corresponding increase in FeAL-1 signal across all cell lines, with the most robust response noted at the highest hepcidin concentration of 4 μg/mL and in the HCT116-luc and SW1990-luc lines (Figure 5A–D). This effect is consistent with modulation of the hepcidin–ferroportin axis, leading to a reduction in cellular iron export. Control experiments showed, as expected, that similar treatment with FAC, FAS, hepcidin and/or BPY had no effect on bioluminescence in D-luciferin treated cells (Figures S4).

Pharmacokinetic Profile and *In Vivo* Stability of FeAL-1.

We performed pharmacokinetic studies to validate FeAL-1 for *in vivo* studies, and to identify suitable dosing protocols. We administered a single 20 mg/kg dose of FeAL-1 to healthy, immunocompetent C57BL6 mice via intraperitoneal (IP) injection. Blood samples were collected, and plasma analyzed by LC-MS/MS, revealing a peak plasma concentration (C_{max}) of 5.91 μM and a maximum FeAL-1 plasma concentration (T_{max}) at 1 hr. Blood and plasma samples from the same PK study were also assessed for released D-luciferin, which amounted to ca. 19% of the FeAL-1 dose by AUC units (Table S1). Whilst this systemic release of D-luciferin was undesirable, the use of a relatively early time point for imaging combined with normalization of the FeAL-1 signal, overcame this issue, as detailed below.

FeAL-1 Detects Changes to Hepatic LIP in Healthy Liver Tissue Following Hepcidin or Doxorubicin Treatment.

We next asked whether FeAL-1 could detect physiologically relevant changes to LIP in mouse tissues *in vivo*. We selected the liver as a model organ for these studies due to the important role of the liver and hepatic hepcidin in regulating systemic iron homeostasis[2] and secondly, because a convenient method is available to achieve selective luciferase expression in mouse liver using the hydrodynamic transgene delivery method[50,51]. To enable normalization of the FeAL-1 response to luciferase expression levels in individual animals,

we used a dual-reporter encoding both *Renilla* luciferase (Rluc) and firefly luciferase (Fluc) on the same plasmid[52]. In this system, Rluc serves as an orthogonal control of reporter expression level, since its cognate substrate coelenterazine does not cross-react with firefly luciferase[53]. Liver-specific transgene expression was achieved by hydrodynamic injection of 5–10 μg of plasmid DNA (addgene #101139) in 1.5 mL in saline into the tail vein of mice in ≤5 seconds, and waiting ~8 hours for optimal transgene expression[50].

Informed by its PK profile, we developed an optimized dosing and imaging protocol for FeAL-1and validated its iron-dependent response by pre-treating mice with hepcidin to effect a predicted expansion of hepatic LIP. Accordingly, we administered synthetic human hepcidin to mice at 50 μg/mouse/day for three days as described[54] prior to tail-vein injection of Fluc/Rluc plasmid DNA (Table S2). A second cohort of control mice received no hepcidin treatment prior to injection of plasmid DNA. After waiting 8 hours for transgene expression to be established, mice were administered the Rluc substrate coelenterazine (30 μg/animal) and imaged on an IVIS whole-body bioluminescent imager (PerkinElmer, Inc.). Then, allowing three hours for coelenterazine elimination, a single 36 mg/kg dose of FeAL-1 was administered via IP injection and the mice imaged 25 minutes later. Finally, mice were imaged a third time the following day, 5 minutes after IP injection of a single 36 mg/kg dose of D-luciferin. This protocol allowed normalization of FeAL-1 signal to either Rluc signal (i.e., from the coelenterazine injection) or Fluc signal (from the final D-luciferin injection). As expected, the normalized bioluminescent response of FeAL-1 was significantly higher in hepcidin-treated mice than in the control group that received no hepcidin treatment. Similar results were obtained when the FeAL-1 signal was normalized to coelenterazine (Rluc) or to the D-luciferin (Fluc) baseline responses (i.e., FeAL-1 Fluc/Rluc or FeAL-1 Fluc/Fluc, Figure 6A, B). Imaging with FeAL-1 therefore confirmed the expected physiological effect of hepcidin treatment on LIP in healthy mouse livers and provided validation of the new probe for *in vivo* studies of LIP.

Next, we used FeAL-1 and the same dual-reporter liver model to explore LIP in the livers of mice treated with the anthracycline anti-cancer agent doxorubicin (DOX). The clinical utility of anthracyclines is limited by cardiomyopathy[55], with a recent study linking these effects to upregulation of heme degradation pathways and the induction of ferroptosis in cardiomyocytes[16]. The same study also reported a modest (≤2-fold) elevation of “non-heme” iron in the liver, spleen, kidneys, and blood, of DOX-treated mice using an *ex vivo* methodology that is not sensitive to iron oxidation state[16]. To evaluate whether DOX treatment elevates hepatic LIP, we treated NSG mice with a single dose of DOX (10 mg/kg, IP) five days prior to hydrodynamic tail vein injection of the Fluc/Rluc-encoding plasmid DNA. We administered coelenterazine (30 μg/animal), FeAL-1 (36 mg/kg) and D-luciferin (36 mg/kg) according to our optimized protocol (Table S2) and imaged the mice as before. We noted a significant 2- to 3-fold increase in the normalized bioluminescence signal of FeAL-1 in DOX-treated mice as compared to a control group, consistent with the reported[16] elevation of “non-heme iron” using *ex vivo* analysis, but now in live mice and with oxidation state specificity (Figure 6A, B).

To further explore our findings with FeAL-1 in hepcidin- and DOX-treated mice, we performed immunohistochemical (IHC) staining of livers removed from the same mice

imaged with FeAL-1. As expected, we observed reduced ferroportin staining in the livers of hepcidin-treated groups compared to untreated controls, but unexpectedly also saw reduced ferroportin staining in liver slices of DOX-treated animals, as compared to controls (Figure 6C and Figure S5). Since DOX treatment was proposed to induce ferroptosis in cardiomyocytes[16], we next stained the hearts and livers of mice from all three study arms for 4-hydroxynonenal (4-HNE), a byproduct of lipid peroxidation and biomarker of ferroptosis[56]. We found the livers of both hepcidin- and DOX-treated mice showed increased staining for 4-HNE as compared to the control group, while the heart tissue of DOX-treated, but not hepcidin-treated mice, showed increased 4-HNE staining over untreated controls (Figure 6C and Figure S5).

Overall, the live imaging studies with FeAL-1 confirmed the predicted effect of hepcidin in reducing liver ferroportin levels, with a concomitant elevation of LIP in this organ. These studies also provided the first *in vivo* evidence that labile Fe^{2+} is elevated in the livers of mice treated with DOX, and furthermore, that this effect may derive from perturbation of the hepcidin-ferroportin axis. Given that iron dyshomeostasis and ferroptosis are implicated in liver disease[57,58], the possibility that DOX therapy elevates hepatic labile iron could have implications for the therapeutic use of this drug in certain populations.

FeAL-1 Reveals Elevated Labile Iron in PDA Tumor Models *In Vivo*.

We next used FeAL-1 to evaluate Fe^{2+} levels in orthotopic PDA xenograft models, a tumor type that has been associated with elevated LIP[59]. Dual-reporter mouse PDA models were established by orthotopic implantation in the pancreas of Fluc/Rluc expressing MIA PaCa-2, SW1990, or FC1245 cells and the cohorts monitored for tumor growth. When tumors were established, mice were sequentially treated IP with coelenterazine (30 μg/mouse), FeAL-1 (36 mg/kg), and D-luciferin (36 mg/kg) and then imaged after each treatment according to the previously established protocol. The normalized FeAL-1 Fluc/Rluc response was ~2.1 (MIA PaCa-2), ~1.7 (SW1990), and ~0.7 (FC1245) in the three PDA models (Figure 7A, B, C). Thus, MIA PaCa-2 tumors had the highest FeAL-1 response, while all three tumor types showed substantially higher normalized FeAL-1 Fluc/Rluc response than in the livers of non-tumor bearing mice studied above (Figure 7D). The finding that normalized FeAL-1 response in PDA tumors can substantially exceed that in healthy liver is notable, given that liver is the major organ of iron storage and regulation in mammalian physiology.

We next asked whether labile Fe^{2+} in PDA models could be elevated even further by hepcidin treatment. We treated tumor bearing mice with hepcidin (50 μg/mouse) for three days prior to sequential administration of probes and imaging per the standard protocol. We observed robust increases in FeAL-1 response in all three PDA tumor models pre-treated with hepcidin, with the MIA PaCa-2 and SW1990 returning a FeAL-1 Fluc/Rluc response of ~5, a value 2–3-fold higher than in untreated controls (Figure 7). In fact, the magnitude of the hepcidin effect in tumor was similar to that observed in liver (Figure 6A and B), even though basal FeAL-1 signal was significantly higher in tumor than liver (Figure 7D). Staining the FC1245 tumors of two xenograft mice for ferroportin revealed that the hepcidin-treated animal showed decreased tumoral ferroportin expression relative to the untreated control animal, albeit in only a single comparison (Figure S6). It bears noting

that while hepcidin treatment measurably increased LIP in FC1245 tumors (Figure 7C), the effect was less significant than in the other tumor types. Further study will be required to discern the effects of hepcidin treatment on ferroportin levels in PDA and other xenografts. Finally, staining of FC1245 tumors with the ferroptosis marker 4-HNE was not significantly different in the hepcidin treated and untreated controls (Figure S6 and S7).

Discussion

Labile ferrous iron comprises the soluble and mobile currency of iron in the cell and as such, is a crucial metabolite to understand in the context of cell proliferation, oxidative stress, and vulnerability to ferroptosis. While several reactivity-based probes of cellular iron are now available and widely used in the community, *in vivo* imaging of LIP is still relatively unexplored. Here, we describe FeAL-1, a next-generation probe of Fe^{2+} for use in luciferase expressing cells and live animals. We found that the release of D-luciferin from FeAL-1 proceeds with high selectivity for Fe^{2+} over Fe^{3+} and other metal ions or cellular reductants, and that FeAL-1 signal is more robust than that of first-generation probe ICL-1. We showed that FeAL-1 can detect changes in intracellular Fe^{2+} levels in cancer cell lines subjected to iron supplementation, chelation, or the action of hepcidin. For *in vivo* studies, we employed a dual luciferase reporter system and confirmed the predicted effects of hepcidin administration on the elevation of hepatic labile iron, as judged by FeAL-1 signal normalized to luciferase expression in each animal. Finally, we showed that hepcidin treatment can elevate labile iron in PDA tumor xenografts, and that doxorubicin treatment elevates labile iron in liver leading to increased lipid peroxidation, a pivotal event in ferroptotic cell death.

The results of our xenografts provide further evidence in support of an emerging narrative around “iron addicted” tumors[6,8,59]. Application of FeAL-1 enabled a semi-quantitative assessment of LIP in the iron-addicted tumor phenotype to that of hepatic LIP in non-tumor bearing mice, with some orthotopic PDA models (e.g. MiaPaCa-2) eliciting a normalized luminescence signal ~10-fold greater than that of healthy liver. This is a significant finding in light of current interest in ferroptosis-inducing therapeutics in oncology[8,11,60–63] and in drug conjugates that target iron avid tumors[59,64–69]. Overall, our findings showcase the utility of FeAL-1 as an *in vivo* probe of tumor Fe^{2+} and suggest that its application may be extended to study physiological Fe^{2+} flux in response to various drug treatments or other stimuli. Given the increasingly apparent role of Fe^{2+} and ferroptosis in diverse disease states, new tools like FeAL-1 will be invaluable in helping uncover the contributions of labile ferrous iron across biological processes and disease pathologies.

Limitations of the study

Imaging with FeAL-1 requires the genetic introduction of a luciferase reporter in cells or tissues of animals to be studied. Expression levels of the luciferase reporter will vary between different animals and these differences will impact the FeAL-1 bioluminescent signal. Also, drug or other treatments can in principle alter the enzymatic activity of the luciferase reporter in ways that would impact the FeAL-1 response. To mitigate these effects, normalization to Fluc or Rluc signal from the same animals is critical. Normalized

FeAL-1 response is a ratio and comparing normalized values (ratios) between experiments or conditions provides an only semi-quantitative measure of LIP. Normalized FeAL-1 signal cannot currently be used to determine absolute LIP concentrations. We strongly recommend that FeAL-1 be administered by the intraperitoneal route using the formulation described. The oral bioavailability of FeAL-1 has not been examined, and formulation for the intravenous route has not been explored. While luciferase expressing mice are available from commercial sources, it may be technically challenging to introduce luciferase reporters into specialized, genetically engineered mice required for some disease models.

Significance

Dysregulated iron metabolism and iron-dependent cell death (ferroptosis) have been associated with diverse disease pathologies, including neurodegeneration, ischemia-reperfusion injury, and cancer. However, the *in vivo* imaging of iron flux in animals and disease models is mostly unknown due to a lack of reliable chemical tools and approaches to interrogate this mobile, redox-active species. To develop a chemical probe to enable such studies, we leveraged a trioxolane-based sensor of ferrous iron conjugated via a metabolically stable linker to D-luciferin. The resulting probe, Ferrous Iron Activatable Luciferin-1 (FeAL-1), can be applied in standard bioluminescent imaging protocols in luciferase expressing cells and animals. To validate FeAL-1 *in vivo*, we used a dual luciferase reporter system in mouse xenografts and healthy liver, normalizing the FeAL-1 response to that arising from separate D-luciferin or coelenterazine treatments. Comparative *in vivo* imaging using FeAL-1 revealed that pancreatic tumors can accumulate labile iron to an extent that exceeds that of liver and is further elevated by hepcidin treatment. These results suggest possible avenues to 'prime' tumors for subsequent therapy with ferroptosis inducers, or iron-activated cancer therapeutics. We also found with FeAL-1 that doxorubicin treatment elevates labile iron in cardiac tissue and in liver, as was noted in prior *ex vivo* studies of tissues from doxorubicin-treated animals. Overall, live imaging with FeAL-1 should enable studies of iron metabolism and distribution in experimental animals and disease models

STAR METHODS

Resource availability

Lead contact—All requests for reagents and resources should be directed to the lead contact, Adam Renslo (adam.renslo@ucsf.edu)

Materials availability—The FeAL-1 probe described in this study will be made available from the lead contact upon request, contingent on availability of material and execution of a standard materials transfer agreement.

Data and code availability

- All data reported in this paper will be shared by the lead contact.
- This paper does not report original code.

- Any additional information required to analyze the data reported in the paper will be made available from the lead contact upon request.

Experimental Model and Study Participant Details

Cell lines—Human cancer cell lines, HCT116 (ATCC, CCL-247, RRID: CVCL_0291, Male), MIA PaCa-2 (ATCC, CRM-CRL-1420, RRID: CVCL_0428, Male), SW1990 (ATCC, CRL-2172, RRID: CVCL_1723, Male), SW620 (ATCC, CCL-227, RRID: CVCL_0547, Male), Colo357 (ECACC, 94072245, RRID: CVCL_0221, Female) and mouse cancer cell line FC1245 (gift from Dr. David Tuveson) were cultured in complete Dulbecco's Modified Eagle Medium (DMEM, Gibco), supplemented with 10% heat-inactivated fetal bovine serum (FBS) and 1% Penicillin/Streptomycin. All cells were tested negative for mycoplasma contamination. Cells were used within 20 passages from thawing. Cell lines transduced with a lentiviral vector (pCDH-EF1) encoding firefly luciferase and *renilla* luciferase were selected with Puromycin (Thermo) 48hrs after transduction. Transduced cells were expanded with Puromycin for 5–7days before proceeding to *in vitro* and *in vivo* experiments.

Animal models—Nude mice (Nu/J, 002019) were purchased from Jackson lab. Tumor cells labeled with firefly/*renilla* luciferase reporters were subcutaneously injected at 1 × 10^6 cells per flank. Palpable tumors were measured twice a week. Bioluminescent imaging (IVIS, PerkinElmer Inc) was performed until the tumor sizes reached 0.5–1cm. Hydrodynamic tail-vein injections of plasmid DNA were performed as follows: Nude mice (Nu/J) were anesthetized with isoflurane and injected with 10 μg of plasmid DNA suspended in 1.5 mL saline through tail vein in 5 seconds. Bioluminescent imaging (IVIS, PerkinElmer Inc) was performed 8 hours after the injection. Mice were bred and maintained in individually ventilated cages and fed with autoclaved food and sterile water at the University of California, San Francisco (UCSF) Animal Facility. Female (Nu/J) mice (6–8 weeks old) were used for all studies. All experiments were conducted in accordance with protocols approved by the UCSF Institutional Animal Care and Use Committee.

Method details

UPLC-MS Fe^{2+}-Fragmentation Assay—To a 4 mL vial containing a stir bar and 366.4 μL of a 50 mM Tris-HCl buffer pH 7.4 and DMSO solution (9:1), was added 1.6 μL of a 10 mM FeAL-1 DMSO solution, to give a final concentration of 40 μM FeAL-1 in the vial. 8 μL of a 100 mM solution of sodium ascorbate and 8 μL of a 100 mM solution ascorbic acid were added, giving a final concentration of 2 mM for both additives. The solution was heated to 37 °C for 1 min before a 20 μL aliquot was taken and 5 μL injected into the UPLC-MS to act as a hemin-free control. To initiate the Fe^{2+}-dependent fragmentation of FeAL-1, 16 μL of a 10 mM hemin DMSO solution was added, giving a final concentration of 400 μM hemin and a total volume of 400 μL in the reaction vial. The reaction was gently stirred at 37 °C whilst 20 μL aliquots of the reaction mixture were removed at selected time points and 5 μL was injected into the UPLC-MS. Peaks corresponding to FeAL-1 fragmentation products were recorded from UPLC-MS chromatograms at a wavelength of 303 nm and the resulting traces were plotted using GraphPad Prism software.

Cell-free Assays

Fe^{2+}-Titration Assay—10 μL of a 50 μM FeAL-1 DMSO solution was added to the wells of a 96-well plate containing 180 μL of a 50 mM Tris-HCl buffer pH 7.4, to give a final concentration of 2.5 μM FeAL-1 in the well. Next, 10 μL of ferrous ammonium sulfate ($Fe(NH_4)_2(SO_4)_2{\cdot}6H_2O$; FAS) solutions in MQ-water prepared at 20X the final concentration were added to the corresponding wells. For metal-free control wells, 10 μL of a 50 μM FeAL-1 DMSO solution was added to 190 μL of 50 mM Tris-HCl buffer pH 7.4. For 2,2'-bipyridyl (BPY) iron-chelation treatment conditions, 179 μL of 50 mM Tris-HCl buffer pH 7.4 was added to the corresponding wells, followed by 1 μL of 50 mM BPY DMSO solution (giving a final concentration of 250 μM BPY) and finally 10 μL of a 50 μM FeAL-1 DMSO solution. The total volume in all wells was 200 μL. The plate was wrapped in foil and incubated at 37 °C for 2 hours before a 100 μL volume from each well was transferred to the wells of a white F-bottom Lumitrac 96-well plate (Greiner bio-one). Next, 100 μL of a 10 μg/mL solution of luciferase (Sigma-Aldrich) prepared in a filter sterilized solution of 50 mM Tris-HCl buffer, pH 7.4, containing Mg^{2+} ($MgCl_2$) at a final concentration of 10 mM Zn^{2+} ($ZnCl_2$) at a final concentration of 0.1 mM and ATP (Thermo Scientific) at a final concentration of 2 mM, was added to all wells and gently mixed by pipetting. Bioluminescent signals were measured at 5 minutes using a Tecan Infinite 200M Pro fluorescent plate reader at 37 °C. Analogous control experiments to determine response of luciferase activity to various concentrations of FAS were performed by replacing FeAL-1 with 10 μL of a 20 μM solution of D-luciferin free acid, giving a final concentration of 1 μM D-luciferin.

Metal Selectivity Assay—10 μL of a 50 μM FeAL-1 DMSO solution was added to the wells of a 96-well plate containing 180 μL of a 50 mM Tris-HCl buffer pH 7.4, to give a final concentration of 2.5 μM FeAL-1. 10 μL of MQ-water solutions containing various concentrations of different metal ions (FAS, $MgCl_2$, $CaCl_2$, $MnCl_2$, $FeCl_2$, $FeCl_3$, $CoCl_2$, $NiCl_2$, $Cu(MeCN)_4(PF_6)$, $CuCl_2$ and $ZnCl_2$) were added to the corresponding wells. For metal-free control wells, 10 μL of a 50 μM FeAL-1 DMSO solution was added to 190 μL of 50 mM Tris-HCl buffer pH 7.4. The total volume in all wells was 200 μL. The plate was wrapped in foil and incubated at 37 °C for 2 hours before a 100 μL volume from each well was transferred to the wells of a white F-bottom Lumitrac 96-well plate (Greiner bio-one). Next, 100 μL of a 10 μg/mL solution of luciferase (Sigma-Aldrich) prepared as described previously was added to all wells and gently mixed by pipetting. Bioluminescent signals were measured at 5 minutes using a Tecan Infinite 200M Pro fluorescent plate reader at 37 °C. Analogous control experiments to determine response of luciferase activity to various metal-ion treatments were performed by replacing FeAL-1 with 10 μL of a 20 μM solution of D-luciferin free acid (Gold Biotechnology), giving a final concentration of 1 μM D-luciferin.

Sensitivity to Biologically Redox Active Species and Reductants assay—10 μL of a 50 μM FeAL-1 DMSO solution was added to the wells of a 96-well plate containing 180 μL of a 50 mM Tris-HCl buffer pH 7.4, to give a final concentration of 2.5 μM FeAL-1 in the well. For ApoTF and HoloTf treatment wells, 174 μL of 50 mM Tris-HCl buffer pH 7.4 was added, followed by 10 μL of a 50 μM FeAL-1 DMSO solution. For metal-free

control wells, 10 μL of a 50 μM FeAL-1 DMSO solution was added to 190 μL of 50 mM Tris-HCl buffer pH 7.4. MQ-water solutions of biologically-relevant metals and reductants were added at the following concentrations to the corresponding wells, final concentrations are shown in parentheses: 10 μL of 20X FAS stock (100 μM), 16 μL of 12.5X ApoTf stock (100 μM), 16 μL of 12.5X HoloTf stock (100 μM), 10 μL of 20X FAC stock (1 mM), 10 μL of 20X GSH stock (1 mM), 10 μL of 20X NAC stock (1 mM), 10 μL of 20X BME stock (1 mM), 10 μL of 20X ascorbic acid stock (1 mM) and 10 μL of 20X *t*-BuOOH prepared from a 70% solution in water (1 mM). The total volume in all wells was 200 μL. The plate was wrapped in foil and incubated at 37 °C for 30 mins before a 100 μL volume from each well was transferred to the wells of a white F-bottom Lumitrac 96-well plate (Greiner bio-one). Next, 100 μL of a 10 μg/mL solution of luciferase (Sigma-Aldrich) prepared as described previously was added to all wells and gently mixed by pipetting. Bioluminescent signals were measured at 5 minutes using a Tecan Infinite 200M Pro fluorescent plate reader at 37 °C. Analogous control experiments to determine response of luciferase activity to aforementioned treatments were performed by replacing FeAL-1 with 10 μL of a 20 μM solution of D-luciferin free acid (Gold Biotechnology), giving a final concentration of 1 μM D-luciferin.

FeAL-1 vs. ICL-1 Fe^{2+}-Titration Assay—10 μL of a 100 μM FeAL-1 DMSO solution was added to the wells of a 96-well plate containing 180 μL of 50 mM Hepes buffer, to give a final concentration of 5 μM FeAL-1 in the well. Next, 10 uL of FAS solutions in MQ-water prepared at 20X the final concentration were added to the corresponding wells. For metal-free control wells, 10 μL of a 100 μM FeAL-1 DMSO solution was added to 190 μL of 50 mM Hepes buffer. For D-luciferin control wells, 4 μL of a 5 μM solution of D-luciferin potassium salt was added to 196 μL of 50 mM Hepes buffer, giving a final concentration of 100 nM D-luciferin. The total volume in all wells was 200 μL. The plate was wrapped in foil and incubated at room temperature for 90 mins before 40 μL of each well was transferred to the wells of a white F-bottom Lumitrac 96-well plate (Greiner bio-one). Next, 40 μL of a 100 μg/mL solution of luciferase (Sigma-Aldrich) prepared as described above, was added to all wells and gently mixed by pipetting. Bioluminescent signals were measured at 1 minute and 6 minutes after luciferase addition using a BioTek Synergy H4 Microplate Reader (BioTek Instruments, Inc.) at 37 °C. An analogous experiment to compare the luminescent response of ICL-1 to treatment with FAS was performed replacing by FeAL-1 with 10 μL of a 100 μM ICL-1 DMSO solution, giving a final concentration of 5 μM ICL-1.

Cellular Assays—Luciferase expressing cell lines were cultured in DMEM containing 10% FBS and were passaged and plated in clear-bottom black 96-well plates (Corning Inc, USA) to achieve 75% confluence one day after plating with assaying and imaging taking place two days after plating. Prior to imaging, serum-containing media was aspirated from the cells and replaced with 95 μL serum-free DMEM, followed by 5 μL of ferric ammonium citrate (FAC) prepared in MQ water at 20X final concentration of treatment) and the cells incubated at 37 °C. For iron-chelation treatments using BPY, 5 μL of serum-free DMEM or FAC containing DMEM solution was removed after the 60 minutes incubation at 37 °C and a BPY solution at 20X final concentration of treatment added (prepared by first making a 2000X stock in DMSO with heating and sonication to solubilize, then diluting 100-fold

with Milli-Q water to give a 20X solution). Cells were then returned to the incubator for 30 minutes BPY incubation prior to imaging. Finally, cells were aspirated of iron- and/or chelator-containing media and media replaced with 100 μL of a 75 μM solution of FeAL-1 (prepared by first making a 10 mM solution in DMSO then diluting 133-fold with Ca^{2+}-, Mg^{2+}- free HBSS). Cells were returned to the incubator at 37 °C for 25 minutes and imaged at 30 minutes using the IVIS imaging system (PerkinElmer Inc).

For hepcidin treatments, hepcidin-25 trifluoroacetate (VWR catalog # H-5926.1000BA) was prepared at 1 mg/mL in MQ water then further diluted to give final concentrations of 1, 2 or 4 μg/mL in treatment wells. Cells were returned to incubation at 37 °C for 16 hours prior to adding iron- and/or chelator-treatments as described previously. Analogous control experiments replacing FeAL-1 with 100 μL of D-luciferin free-acid solution at 25 μM final concentration (prepared by first making a 10 mM stock in DMSO and diluting 25-fold in Ca^{2+}-, Mg^{2+}- free HBSS). Cells treated with D-luciferin were incubated at 37 °C for five minutes before being imaged as described previously.

Cellular Assays Comparing FeAL-1 and ICL-1 Response—MiaPaCa2-Luc and SW1990-Luc cells were cultured in DMEM containing 10% FBS and 1% Penicillin-Streptomycin were passaged and plated in clear-bottom black 96-well plates (Greiner Bio-One, USA) to achieve 75% confluence one day after plating. Two days after plating, and 90 minutes prior to addition of probe, serum-containing media was aspirated from the cells and replaced with 95 μL serum-free DMEM, followed by 5 μL of either serum free DMEM or FAC stock solutions (prepared using UltraPure water at 20X final concentration of treatment) and the cells incubated at 37 °C. Iron-chelation treatments using BPY were performed by removing 5 μL of FAC-containing DMEM solution after 60 minutes incubation at 37 °C and replacing with 5 μL of BPY solution prepared at 20X final concentration of treatment (prepared by making a 2000X stock in DMSO with heating and sonication to solubilize, then diluting 100-fold with UltraPure water to give a 20X solution). Cells were then returned to the incubator for 30 minutes prior to imaging. At the end of the 90-minute FAC-incubation time at 37 °C, cells were aspirated of iron- and/or chelator-containing media and replaced with 100 μL of a 20 μM solution of FeAL-1 or ICL-1 (prepared by first making a 1 mM DMSO solution and then diluting 50-fold in Ca^{2+}-, Mg^{2+}- free HBSS). Cells were returned to the incubator at 37 °C for 25 minutes and then imaged immediately at 37 °C using the BioTek Synergy H4 Microplate Reader (BioTek Instruments, Inc.)

Pharmacokinetic studies—The healthy C57BL/6 mice used for this pharmacokinetic study were housed in groups at an Association for Assessment and Accreditation of Laboratory Animal Care (AAALAC) International – accredited facility. The animal research protocol was reviewed and approved by the Merck Institutional Animal Care and Use Committee (IACUC). The mice were cared for in accordance with the Guide for the Care and Use of Laboratory Animals, 8^{th} Edition. They were housed in individual ventilated caging system on an irradiated corncob bedding. A 12-hour light/dark cycle, an ambient temperature of 68–79°F and humidity of 30%–70% was maintained in the animal holding

rooms. The mice had ad libitum access to irradiated pelleted feed and reverse-osmosis–chlorinated water and their cages were changed biweekly.

FeAL-1 was formulated in a dosing vehicle containing 10% DMSO, 50% PEG400, and 40% of a 20% of beta-hydroxypropyl cyclodextrin at 8 mg/mL for the 20 mg/kg dosing arm. A dose volume of 2.5 mL/kg was administered each to 15 mice per group at an average animal weight of 0.021 kg for both treatment groups. Plasma samples were collected by composite sampling: 5, 10, 15, 30, and 45 min samples were taken via orbital bleed from different animals (n=3 at each timepoint) followed by 1, 2, 3, 4, and 7 hour samples taken terminally via vena cava. For orbital bleed, the mice were exposed to isofluarane at appropriate times; and blood collected into EDTA collection tubes, and for terminal bleeds, the mice were exposed to CO_2; and blood immediately collected via vena cava. The blood samples were then centrifuged to separate red blood cells (RBC) and plasma. The RBCs were discarded while 100 μL of supernatant plasma was pipetted into matrix tubes containing 50 μL of saturated (10 mg/mL) sodium fluoride used to prevent the ex vivo biotransformation of FeAL-1. All plasma samples were frozen at −70 °C at all times until LC-MS/MS analysis.

LC-MS/MS analysis of PK Samples—Stock solutions of FeAL-1 and D-luciferin were prepared fresh daily at 10 mM in dimethyl sulfoxide from two separate weighing. Triplicate calibration standards were prepared by dispensing different volumes (ranging from 0.02 to 500 nL) of 1 mM and 0.05 mM working solutions in DMSO using the HP D300 Digital Dispenser. Blank plasma (50 μL) was then added and shaken on a Thermofisher Mixer C for 30 secs. Unknown samples obtained from dosed animals and calibration standards were prepared for LC-MS/MS analysis by a single step protein precipitation with 200 μL of crash solvent containing internal standard (IS) to 50 μL aliquots of individual samples and calibration standards. The internal standard solution was prepared by diluting a 1 mL ampoule of Cerilliant IS MIX (diclofenac 200 μM, labetalol 200 μM, and imipramine 200 μM) in 1 L of acetonitrile containing 0.1% formic acid. For homogeneity, the samples were mixed by gentle vortexing for 1 min and centrifuged at 4200 rpm for 5 min. The supernatant was transferred into a 96-well plate, diluted at a ratio of 1:1 with 0.1% formic acid in water and 10 μL injected into the LC-MS/MS for analysis.

Chromatography was carried out on a Waters Acquity i-class UPLC system equipped with Waters i-class Binary Pumps and a Waters SM-FTN autosampler refrigerated at 10 °C during analysis. Chromatographic separation was achieved with a Waters Acquity HSS T3 (2.1 mm × 50mm, 1.8 μm) C_{18} column maintained at 40 °C. The mobile phase consisting of a solvent A (0.1% formic acid in water) and solvent B (0.1% formic acid in acetonitrile) was delivered at a flow rate of 0.75 mL/min. The LC gradient started from 95/5 (A/B) and changed to 5/95 (A/B) from 0.25 to 1.75 min (ramp) and maintained at this ratio for 0.42 min (step). It was then decreased to 95/5 (A/B) at 2.17 min (step) maintained at this ratio for 1.0 min.

Ion detection was carried out using a triple quadrupole tandem mass spectrometer (API 4500, AB Sciex) equipped with an electrospray interface (ESI). Ions were created in the positive ion mode setting the sprayer voltage at 4.5 kV and the ion source temperature at 500 °C. The common parameters and the nitrogen flow values were set as follows: 50 for

nebulizer gas (Gas 1), 60 for auxiliary gas (Gas 2), 40 for curtain gas and 8 for gas for collision-activated dissociation (CAD) gas respectively. Detection of FeAL-1 and D-luciferin was performed in the multiple reaction-monitoring (MRM) mode using the following precursor to product ion pairs for quantitation: m/z 701.135 → 281.000 (DP/CE: 66/49) for FeAL-1 and m/z 280.875 → 234.900 (DP/CE: 51/29) for D-luciferin. The following MRM transitions were monitored for the internal standards diclofenac, labetalol and imipramine: 329.200 → 162.100 (DP/CE: 76/37); 296.000 → 214.000 (DP/CE: 76/49) and 281.3 → 193.1 (DP/CE: 70/50), respectively. Analyst 1.6.3 (AB Sciex) was used to control the MS-MS system and MultiQuant 3.0.3 (AB Sciex) for data analyses.

Pharmacokinetic Analysis—Pharmacokinetic parameters were obtained by non-compartmental analysis using Watson® LIMS version 7.4.1 (Thermo Fisher Scientific). The area under the plasma concentration-time curve ($AUC_{0\text{-}t}$) was calculated using the linear/log-linear trapezoidal rule from the first time point (0 min) up to the last time point with measurable FeAL-1 concentration. The remaining part of the AUC was estimated by dividing the observed concentration at the last time point by the elimination rate constant (ke). This value was added to $AUC_{0\text{-}t}$ to estimate the $AUC_{0\text{-}inf}$. The percentage AUC extrapolated was a function of $(AUC_{0\text{-}inf} - AUC_{0\text{-}t}) \cdot 100/AUC_{0\text{-}inf}$. The maximum plasma concentration (C_{max}) and the corresponding time at which C_{max} (T_{max}) were obtained by inspection of the plasma concentration-time data.

Histological Analysis—Immunohistochemistry staining was performed on 4-μm-thick sections of 4% paraformaldehyde-fixed and paraffin-embedded tissues. Liver, heart and tumor sections were stained with anti-4 Hydroxynonenal antibody (1:500) and anti-Ferroportin/SLC40A1 Antibody (1:500). Quantification of staining intensity was performed using the IHC Profiler plugin as described by Varghese et at[70] using the digital image analysis software ImageJ[71].

Chemical Reagents and Materials—All chemical reagents were obtained commercially and were used without further purification, unless otherwise stated. Anhydrous solvents were purchased from Sigma-Aldrich and were used without further purification. Solvents used for flash column chromatography and reaction workup procedures were purchased from either Sigma-Aldrich or Fisher Scientific. Column chromatography was performed on Silicycle Sili-prep cartridges using a Biotage Isolera Four automated flash chromatography system.

Instrumentation—NMR spectra were recorded on either a Varian INOVA 400 MHz spectrometer (with 5 mm QuadNuclear Z-Grad Probe), calibrated to $CH(D)Cl_3$ as an internal reference (7.27 and 77.00 ppm for 1H and ^{13}C NMR spectra, respectively). Data for ^{1}H NMR spectra are reported in terms of chemical shift (δ, ppm), multiplicity, coupling constant (Hz), and integration. Data for ^{13}C NMR spectra are reported in terms of chemical shift (δ, ppm), with multiplicity. The following abbreviations are used to denote the multiplicities: s = singlet, d = doublet, t = triplet, q = quartet, m = multiplet, br = broad, app = apparent, or combinations thereof. UPLC–MS and compound purity were determined using a Waters Acquity QDa mass spectrometer equipped with FTN-H Sample

Manager, Evaporative Light Scattering Detector and Photodiode Array Detector. Separations were carried out with Acquity UPLC® BEH C18, 1.7mm, 2.1 × 50 mm column, at 25 °C using a mobile phase of water-acetonitrile containing a constant 0.05 % formic acid. HPLC was performed on a Waters 2535 Separation Module with a Waters 2998 Photodiode Array Detector using an XBridge BEH C18, 3.5μm, 4.6 × 20 mm column, at ambient temperature (unregulated) using a mobile phase of water-methanol containing a constant 0.05 % formic acid. High-resolution mass spectra (HRMS) were obtained using a Finnigan LTQFT mass spectrometer by the mass spectrometry facility at the University of California, Berkeley. All compounds synthesized were ≥95% pure as determined by ^{1}H and ^{13}C NMR and UPLC-MS. Selected solvents were deoxygenated using freeze-pump thaw method and used immediately.

Synthesis of *tert*-butyl ((*R,R*)-dispiro[adamantane-2,3'-[1,2,4]trioxolane-5',1''-cyclohexan]-3''-yl) ethane-1,2-diylbis(methylcarbamate) (2).—To an Ar(g) purged flask containing (*R,R*)-dispiro[adamantane-2,3'-[1,2,4]trioxolane-5',1''-cyclohexan]-3''-yl (4-nitrophenyl) carbonate (**1**)[72] (2.11 g, 2.24 mmol, 1.0 equiv) was added anhydrous CH_2Cl_2 (30 mL) followed by triethylamine (1.0 mL, 7.18 mmol, 3.2 equiv) and *tert*-butyl methyl(2-(methylamino)ethyl)carbamate (2.11 g, 11.2 mmol, 5.0 equiv). The reaction mixture was stirred at rt for 30 min and was deemed complete by TLC (50% EtOAc–Hexanes, product R_f = 0.49, stains dark blue with CAM). EtOAc (200 mL) and DI water (50 mL) were added and the organic phase was washed repeatedly with 1M aq. Na_2CO_3 (7 × 30 mL) until the aq layer was colorless (indicating that most of the *p*-nitrophenol had been removed from the organic layer). The combined organic layers were washed with brine (1 × 150 mL), dried ($MgSO_4$), filtered and concentrated *in vacuo* to a crude yellow oil. Purification via flash column chromatography (120 g silicycle column, 0–25 % EtOAc–Hexanes, product eluted at 19% EtOAc–Hexanes) afforded the title compound **2** (1.10 g, 2.22 mmol, 99%) as a colorless solid. ^{1}H NMR (400 MHz, $CDCl_3$) δ 4.69 (br s, 1H), 3.17 – 3.55 (m, 4H), 2.75 – 2.92 (m, 6H), 2.05 – 2.26 (m, 2H), 1.81 – 1.95 (m, 7H), 1.64 – 1.79 (m, 7H), 1.43 – 1.61 (m, 4H), 1.40 (s, 9H), 1.07 – 1.35 (m, 2H); ^{13}C NMR (100 MHz, $CDCl_3$)[1] δ 155.5 (multiple peaks), 111.5, 108.6, 79.5 (multiple peaks), 69.4, 53.9, 47.0, 46.6, 46.4, 46.2, 45.8, 40.0, 39.9, 39.7, 36.2, 36.2, 34.8, 34.7, 34.6, 34.6, 34.4, 34.0, 33.9, 37.7, 30.8, 30.7, 29.2, 28.4, 26.8, 26.4, 19.6, 19.5; MS (ESI) calcd for $C_{26}H_{42}N_2O_7Na$ $[M + Na]^+$: m/z 517.29 found: 517.18. Duplication of some signals in the ^{13}C-NMR spectrum of compound **2** are attributed to slow interconversion of *N,N'*-dimethylethylene-diamine carbamate rotamers on the NMR timescale. The use of VT-NMR to coalesce rotameric resonances was not possible due to instability of **2** at elevated temperatures.

Synthesis of (*R,R*)-dispiro[adamantane-2,3'-[1,2,4]trioxolane-5',1''-cyclohexan]-3''-yl methyl(2-(methylamino)ethyl)carbamate hydrochloride salt (3).—To an Ar(g) purged flask containing intermediate **2** (1.10 g, 2.22 mmol, 1.0 equiv) was added anhydrous MeOH (144 mL) and the mixture cooled to 0 °C before acetyl chloride (7.12 mL, 100 mmol, 45.0 equiv) was added dropwise. The reaction mixture was stirred at 0 °C for 10 min before being allowed to gradually warm to rt for 12.5 h. Upon completion, the reaction mixture was concentrated *in vacuo* to a gummy semi-solid. Azeotropic distillation under reduced pressure with MeOH (2 × 30 mL), followed by Et_2O (2 × 20 mL) afforded

intermediate **3** (970 mg, 2.25 mmol, quantitative yield) as a colorless solid that was used directly in the next step without further purification. MS (ESI) calcd for $C_{21}H_{35}N_2O_5$ [M + H]$^+$: m/z 395.25 found: 395.24. Note: purification of this material is not necessary, nor is it recommended as the compound is prone to undergo cyclization upon neutralization of the amine salt.

Synthesis of 2-cyanobenzo[*d*]thiazol-6-yl ((*R,R*)-dispiro[adamantane-2,3'-[1,2,4]trioxolane-5',1''-cyclohexan]-3''-yl) ethane-1,2-diylbis(methylcarbamate) (6).—To an Ar(g) purged flask containing 2-cyano-6-hydroxybenzothiazole benzothiazole (**4**) (192 mg, 1.09 mmol, 1.0 equiv) and anhydrous THF (21 mL) cooled to 0 °C, was added 4-nitrophenyl chloroformate (220 mg, 1.09 mmol, 1.0 equiv) and triethylamine (760 uL, 5.45 mmol, 5.0 equiv). The reaction was stirred at 0 °C for 2.5 h until formation of carbonate intermediate **5** was confirmed by UPLC-MS. The reaction was transferred to a separate Ar(g) purged flask containing compound **3** (470 mg, 1.09 mmol, 1.0 equiv) using additional anhydrous THF (8 mL) to complete the transfer, the solution immediately turned dark red/brown. After 50 min, the reaction was judged complete and the mixtureconcentrated under reduced pressure to an orange semi-solid. The crude residue was purified by preparative HPLC (70–90% MeCN–deoxygenated MQ-water) and the product-bearing fractions were concentrated *in vacuo* to afford the title compound **6** (335.5 mg, 0.56 mmol, 52%) as a colorless solid. ^{1}H NMR (400 MHz, MeOD)[1] δ 8.17 – 8.26 (m, 1H), 7.92 – 8.01 (m, 1H), 7.48 (app. dt, *J* = 9.0, 2.3 Hz, 1H), 4.64 – 4.79 (m, 1H), 3.42 – 3.87 (m, 4 H), 3.19 (d, *J* = 2.9 Hz, 1H), 2.96 – 3.09 (m, 5H), 2.03 – 2.16 (m, 1H), 1.66 – 2.02 (m, 17H), 1.51 – 1.63 (m, 2H), 1.34 – 1.50 (m, 2H); ^{13}C NMR (100 MHz, MeOD)[1] δ 156.4, 156.2, 156.1, 154.5, 154.4, 151.7, 151.6, 151.6, 149.8, 149.6, 149.6, 137.1, 136.9 (multiple peaks), 136.3, 136.3, 125.0, 125.0, 123.3, 123.1, 123.0, 122.8, 155.1, 114.8, 114.7, 114.7, 112.5, 111.3, 111.2, 111.1, 108.5, 108.5, 71.9, 71.9, 71.7, 71.7, 69.4, 46.7, 46.5, 46.3, 45.8, 45.7, 39.9, 39.8, 39.6, 39.5, 36.3, 36.2, 36.2, 34.4, 34.3 (multiple peaks), 34.2, 33.9 (multiple peaks), 33.7, 33.5, 33.4 (multiple peaks), 30.3, 30.2, 30.2, 29.4 (multiple peaks), 29.3, 29.2, 29.1, 26.9 (multiple peaks), 26.5, 26.5, 25.0, 19.4, 19.4, 19.3, 19.2, 19.2; MS (ESI) calcd for $C_{30}H_{36}N_4O_7SNa$ [M + Na]$^+$: m/z 619.22 found: 619.23. Some duplicate ^{1}H and ^{13}C-NMR resonances in the spectra of compound **6** are attributed to the slow interconversion *N,N'*-dimethylethylene-diamine carbamate rotamers on the NMR timescale. The use of VT-NMR to coalesce rotameric resonances was not possible due to instability of **6** at elevated temperatures.

Synthesis of (*S*)-2-(6-(((2-(((((*R,R*)-dispiro[adamantane-2,3'-[1,2,4]trioxolane-5',1''-cyclohexan]-3''-yl)oxy)carbonyl)(methyl)amino)ethyl)(methyl)carbamoyl)oxy) benzo[*d*]thiazol-2-yl)-4,5-dihydrothiazole-4-carboxylic acid. (7, FeAL-1).—To an Ar(g) purged vial containing D-cysteine hydrochloride monohydrate (24.5 mg, 0.140 mmol, 1.5 equiv) and K_2CO_3 (23.1 mg, 0.167 mmol, 1.8 equiv) was added deoxygenated MQ-water (223 μL), followed by a solution of compound **6** (55.5 mg, 0.093 mmol, 1.0 equiv) in deoxygenated MeOH (674 μL) and deoxygenated CH_2Cl_2 (674 μL). The homogenous solution was stirred at rt for 1 h until UPLC-MS indicated that the reaction was complete. EtOAc (20 mL) and DI water (5 mL) were added and the mixture filtered under vacuum

through a sintered funnel. The filtrate was neutralized with 1 M HCl (140 μL, 0.140 mmol, 1.5 equiv.), diluted with brine (1 mL) and the layers separated. The aqueous phase was back-extracted with EtOAc (3 × 20 mL) with the addition of brine (3 × 5 mL) to aid partitioning of the layers and the combined organic phases washed with brine (1 ×50 mL), dried ($MgSO_4$), filtered and concentrated *in vacuo* to a crude residue. Purification via flash column chromatography (12 g silicycle column, 0–15% MeOH–CH_2Cl_2) afforded the title compound **7** (FeAL-1) (39.9 mg, 0.093 mmol, 61%) as a colorless solid. ^{1}H NMR (400 MHz, MeOD) δ 8.10 (d, *J* = 9.0 Hz, 1H), 7.84 (s, 1H), 7.36 (dd, *J* = 8.9, 2.3 Hz, 1H), 5.31 (br t, *J* = 9.1 Hz, 1H), 4.68 (br s, 1H), 3.76 – 3.82 (m, 2H), 3.56 – 3.73 (m, 3H), 3.42 – 3.52 (m, 1H), 3.18 – 3.22 (m, 1H), 2.97 – 3.09 (m, 5H), 2.21 – 2.33 (m, 1H), 2.08 – 2.16 (m, 1 H), 1.65 – 2.01 (m, 17H), 1.53 – 1.62 (m, 2H), 1.38 – 1.51 (m, 2H); ^{13}C NMR (100 MHz, MeOD)[1] δ 173.5, 172.0 (multiple peaks), 171.5, 166.0, 161.2, 161.1, 161.0, 156.4, 156.2, 156.1, 155.1, 154.8, 154.7, 150.7, 150.5 (multiple peaks), 150.4, 136.6, 136.5, 124.3, 122.0, 121.8, 121.6, 115.1, 114.8, 114.8, 114.7, 111.3, 111.2, 111.1, 108.5, 108.4, 78.4, 74.3, 72.0, 71.9, 71.7, 71.7, 70.7, 69.4, 69.1, 65.4, 62.1, 62.1, 61.8, 60.2, 46.7, 46.5, 46.3, 45.8, 45.7, 39.9, 39.8, 39.7, 39.6, 36.3, 36.2 (multiple peaks), 34.6, 34.3 (multiple peaks), 34.0, 33.8, 33.8, 33.6, 33.6, 33.5, 33.4, 33.3, 31.7, 30.3, 29.4, 29.1 (multiple peaks), 29.0, 28.8, 28.7, 26.9, 26.9. 26.5, 26.5, 25.0, 24.7, 24.6, 24.6, 24.1, 23.7, 23.5, 23.1, 22.7, 22.4, 22.2, 20.7, 19.8, 19.4, 19.4, 19.3, 19.2 (multiple peaks); HRMS (ESI) calcd for $C_{33}H_{40}N_4O_9S_2$ [M + H]$^+$: m/z 701.2310 found: 701.2328.

Multiple resonances for some carbon atoms in the ^{13}C-NMR spectrum of compound **7** are attributed to the slow interconversion of *N,N'*-dimethylethylene-diamine carbamate rotamers on the NMR timescale. The use of VT-NMR to coalesce rotameric resonances was not possible due to instability of **7** at elevated temperatures.

Quantitation and Statistical Analysis

Statistical analysis was performed using GraphPad Prism 9 software. Statistical details are provided in the figure legends and include numbers of replicates and standard deviation (SD) as a measure of precision.

Supplementary Material

Refer to Web version on PubMed Central for supplementary material.

Acknowledgments

This work was funded in part by postdoctoral support (to RLG) from Merck & Co. Inc., and by NIH Grants R01CA260860 (to EAC and ARR) and R01AI105106 (to ARR), and R01GM79465 (to CJC).

References

1. Ganz T, and Nemeth E (2015). Iron homeostasis in host defence and inflammation. Nat. Rev. Immunol. 15, 500–510. 10.1038/nri3863. [PubMed: 26160612]
2. Nemeth E, and Ganz T (2021). Hepcidin-Ferroportin Interaction Controls Systemic Iron Homeostasis. Int. J. Mol. Sci. 22. 10.3390/ijms22126493.
3. Ganz T (2013). Systemic iron homeostasis. Physiol. Rev. 93, 1721–1741. 10.1152/physrev.00008.2013. [PubMed: 24137020]

4. Billesbølle CB, Azumaya CM, Kretsch RC, Powers AS, Gonen S, Schneider S, Arvedson T, Dror RO, Cheng Y, and Manglik A (2020). Structure of hepcidin-bound ferroportin reveals iron homeostatic mechanisms. Nature 586, 807–811. 10.1038/s41586-020-2668-z. [PubMed: 32814342]
5. Manz DH, Blanchette NL, Paul BT, Torti FM, and Torti SV (2016). Iron and cancer: recent insights. Ann. N. Y. Acad. Sci. 1368, 149–161. 10.1111/nyas.13008. [PubMed: 26890363]
6. Basuli D, Tesfay L, Deng Z, Paul B, Yamamoto Y, Ning G, Xian W, McKeon F, Lynch M, Crum CP, et al. (2017). Iron addiction: a novel therapeutic target in ovarian cancer. Oncogene 36, 4089–4099. 10.1038/onc.2017.11. [PubMed: 28319068]
7. Deng Z, Manz DH, Torti SV, and Torti FM (2019). Effects of Ferroportin-Mediated Iron Depletion in Cells Representative of Different Histological Subtypes of Prostate Cancer. Antioxid. Redox Signal. 30, 1043–1061. 10.1089/ars.2017.7023. [PubMed: 29061069]
8. Rodriguez R, Schreiber SL, and Conrad M (2022). Persister cancer cells: Iron addiction and vulnerability to ferroptosis. Mol. Cell 82, 728–740. 10.1016/j.molcel.2021.12.001. [PubMed: 34965379]
9. Galaris D, Barbouti A, and Pantopoulos K (2019). Iron homeostasis and oxidative stress: An intimate relationship. Biochim. Biophys. Acta Mol. Cell Res. 1866, 118535. 10.1016/j.bbamcr.2019.118535. [PubMed: 31446062]
10. Stockwell BR, Friedmann Angeli JP, Bayir H, Bush AI, Conrad M, Dixon SJ, Fulda S, Gascón S, Hatzios SK, Kagan VE, et al. (2017). Ferroptosis: A regulated cell death nexus linking metabolism, redox biology, and disease. Cell 171, 273–285. 10.1016/j.cell.2017.09.021. [PubMed: 28985560]
11. Jiang X, Stockwell BR, and Conrad M (2021). Ferroptosis: mechanisms, biology and role in disease. Nat. Rev. Mol. Cell Biol. 22, 266–282. 10.1038/s41580-020-00324-8. [PubMed: 33495651]
12. Zou Y, and Schreiber SL (2020). Progress in understanding ferroptosis and challenges in its targeting for therapeutic benefit. Cell Chem. Biol. 27, 463–471. 10.1016/j.chembiol.2020.03.015. [PubMed: 32302583]
13. Hangauer MJ, Viswanathan VS, Ryan MJ, Bole D, Eaton JK, Matov A, Galeas J, Dhruv HD, Berens ME, Schreiber SL, et al. (2017). Drug-tolerant persister cancer cells are vulnerable to GPX4 inhibition. Nature 551, 247–250. 10.1038/nature24297. [PubMed: 29088702]
14. Belaidi AA, and Bush AI (2016). Iron neurochemistry in Alzheimer's disease and Parkinson's disease: targets for therapeutics. J. Neurochem. 139 Suppl 1, 179–197. 10.1111/jnc.13425.
15. Tuo QZ, Lei P, Jackman KA, Li XL, Xiong H, Li XL, Liuyang ZY, Roisman L, Zhang ST, Ayton S, et al. (2017). Tau-mediated iron export prevents ferroptotic damage after ischemic stroke. Mol. Psychiatry 22, 1520–1530. 10.1038/mp.2017.171. [PubMed: 28886009]
16. Fang X, Wang H, Han D, Xie E, Yang X, Wei J, Gu S, Gao F, Zhu N, Yin X, et al. (2019). Ferroptosis as a target for protection against cardiomyopathy. Proc Natl Acad Sci USA 116, 2672–2680. 10.1073/pnas.1821022116. [PubMed: 30692261]
17. Irving H, and Williams RJP (1948). Order of stability of metal complexes. Nature 162, 746–747. 10.1038/162746a0.
18. Bruemmer KJ, Crossley SWM, and Chang CJ (2020). Activity-Based Sensing: A Synthetic Methods Approach for Selective Molecular Imaging and Beyond. Angew. Chem. Int. Ed 59, 13734–13762. 10.1002/anie.201909690.
19. Au-Yeung HY, Chan J, Chantarojsiri T, and Chang CJ (2013). Molecular imaging of labile iron(II) pools in living cells with a turn-on fluorescent probe. J. Am. Chem. Soc. 135, 15165–15173. 10.1021/ja4072964. [PubMed: 24063668]
20. Hirayama T (2019). Fluorescent probes for the detection of catalytic Fe(II) ion. Free Radic. Biol. Med. 133, 38–45. 10.1016/j.freeradbiomed.2018.07.004. [PubMed: 29990536]
21. Shao C, Liu Y, Chen Z, Qin Y, Wang X, Wang X, Yan C, Zhu H-L, Zhao J, and Qian Y (2022). 3D two-photon brain imaging reveals dihydroartemisinin exerts antiepileptic effects by modulating iron homeostasis. Cell Chem. Biol. 29, 43–56.e12. 10.1016/j.chembiol.2021.12.006. [PubMed: 34936859]

22. Fontaine SD, DiPasquale AG, and Renslo AR (2014). Efficient and stereocontrolled synthesis of 1,2,4-trioxolanes useful for ferrous iron-dependent drug delivery. Org. Lett. 16, 5776–5779. 10.1021/ol5028392. [PubMed: 25331549]

23. Spangler B, Morgan CW, Fontaine SD, Vander Wal MN, Chang CJ, Wells JA, and Renslo AR (2016). A reactivity-based probe of the intracellular labile ferrous iron pool. Nat. Chem. Biol. 12, 680–685. 10.1038/nchembio.2116. [PubMed: 27376690]

24. Aron AT, Loehr MO, Bogena J, and Chang CJ (2016). An Endoperoxide Reactivity-Based FRET Probe for Ratiometric Fluorescence Imaging of Labile Iron Pools in Living Cells. J. Am. Chem. Soc. 138, 14338–14346. 10.1021/jacs.6b08016. [PubMed: 27768321]

25. Aron AT, Heffern MC, Lonergan ZR, Vander Wal MN, Blank BR, Spangler B, Zhang Y, Park HM, Stahl A, Renslo AR, et al. (2017). In vivo bioluminescence imaging of labile iron accumulation in a murine model of Acinetobacter baumannii infection. Proc Natl Acad Sci USA 114, 12669–12674. 10.1073/pnas.1708747114. [PubMed: 29138321]

26. Muir RK, Zhao N, Wei J, Wang Y-H, Moroz A, Huang Y, Chen Y-C, Sriram R, Kurhanewicz J, Ruggero D, et al. (2019). Measuring Dynamic Changes in the Labile Iron Pool in Vivo with a Reactivity-Based Probe for Positron Emission Tomography. ACS Cent. Sci. 5, 727–736. 10.1021/acscentsci.9b00240. [PubMed: 31041393]

27. Zhao N, Huang Y, Wang Y-H, Muir RK, Chen Y-C, Wei J, Hooshdaran N, Viswanath P, Seo Y, Ruggero D, et al. (2021). Ferronostics: Measuring Tumoral Ferrous Iron with PET to Predict Sensitivity to Iron-Targeted Cancer Therapies. J. Nucl. Med. 62, 949–955. 10.2967/jnumed.120.252460. [PubMed: 33246980]

28. Love AC, and Prescher JA (2020). Seeing (and using) the light: recent developments in bioluminescence technology. Cell Chem. Biol. 27, 904–920. 10.1016/j.chembiol.2020.07.022. [PubMed: 32795417]

29. Li S, Ruan Z, Zhang H, and Xu H (2021). Recent achievements of bioluminescence imaging based on firefly luciferin-luciferase system. Eur. J. Med. Chem. 211, 113111. 10.1016/j.ejmech.2020.113111. [PubMed: 33360804]

30. Su TA, Bruemmer KJ, and Chang CJ (2019). Caged luciferins for bioluminescent activity-based sensing. Curr. Opin. Biotechnol. 60, 198–204. 10.1016/j.copbio.2019.05.002. [PubMed: 31200275]

31. Van de Bittner GC, Dubikovskaya EA, Bertozzi CR, and Chang CJ (2010). In vivo imaging of hydrogen peroxide production in a murine tumor model with a chemoselective bioluminescent reporter. Proc Natl Acad Sci USA 107, 21316–21321. 10.1073/pnas.1012864107. [PubMed: 21115844]

32. Chen P, Zheng Z, Zhu Y, Dong Y, Wang F, and Liang G (2017). Bioluminescent Turn-On Probe for Sensing Hypochlorite in Vitro and in Tumors. Anal. Chem. 89, 5693–5696. 10.1021/acs.analchem.7b01103. [PubMed: 28485134]

33. Mofford DM, Adams ST, Reddy GSKK, Reddy GR, and Miller SC (2015). Luciferin amides enable in vivo bioluminescence detection of endogenous fatty acid amide hydrolase activity. J. Am. Chem. Soc. 137, 8684–8687. 10.1021/jacs.5b04357. [PubMed: 26120870]

34. Porterfield WB, Jones KA, McCutcheon DC, and Prescher JA (2015). A “Caged” Luciferin for Imaging Cell-Cell Contacts. J. Am. Chem. Soc. 137, 8656–8659. 10.1021/jacs.5b02774. [PubMed: 26098396]

35. Luo J, Yang J, Li G, Yang S, Zhou Y, Li J-B, Huang G, Hu Y, Zou S, Zeng Q, et al. (2020). Noncovalently Caged Firefly Luciferins Enable Amplifiable Bioluminescence Sensing of Hyaluronidase-1 Activity in Vivo. ACS Sens. 5, 1726–1733. 10.1021/acssensors.0c00393. [PubMed: 32441104]

36. Feng P, Ma L, Xu F, Gou X, Du L, Ke B, and Li M (2019). In vivo bioluminescence imaging of labile iron pools in a murine model of sepsis with a highly selective probe. Talanta 203, 29–33. 10.1016/j.talanta.2019.05.017. [PubMed: 31202341]

37. Mofford DM, Reddy GR, and Miller SC (2014). Aminoluciferins extend firefly luciferase bioluminescence into the near-infrared and can be preferred substrates over D-luciferin. J. Am. Chem. Soc. 136, 13277–13282. 10.1021/ja505795s. [PubMed: 25208457]

38. Zhang X, Tang K, Wang H, Liu Y, Bao B, Fang Y, Zhang X, and Lu W (2016). Design, Synthesis, and Biological Evaluation of New Cathepsin B-Sensitive Camptothecin Nanoparticles Equipped with a Novel Multifuctional Linker. Bioconjug. Chem. 27, 1267–1275. 10.1021/acs.bioconjchem.6b00099. [PubMed: 27070848]
39. Dal Corso A, Caruso M, Belvisi L, Arosio D, Piarulli U, Albanese C, Gasparri F, Marsiglio A, Sola F, Troiani S, et al. (2015). Synthesis and biological evaluation of RGD peptidomimetic-paclitaxel conjugates bearing lysosomally cleavable linkers. Chem. Eur. J 21, 6921–6929. 10.1002/chem.201500158. [PubMed: 25784522]
40. Jin C, Zhang Q, and Lu W (2017). Synthesis and biological evaluation of hypoxia-activated prodrugs of SN-38. Eur. J. Med. Chem. 132, 135–141. 10.1016/j.ejmech.2017.03.040. [PubMed: 28350997]
41. Miao Q, Yeo DC, Wiraja C, Zhang J, Ning X, Xu C, and Pu K (2018). Near-Infrared Fluorescent Molecular Probe for Sensitive Imaging of Keloid. Angew. Chem. Int. Ed 57, 1256–1260. 10.1002/anie.201710727.
42. Elgersma RC, Coumans RGE, Huijbregts T, Menge WMPB, Joosten JAF, Spijker HJ, de Groot FMH, van der Lee MMC, Ubink R, van den Dobbelsteen DJ, et al. (2015). Design, Synthesis, and Evaluation of Linker-Duocarmycin Payloads: Toward Selection of HER2-Targeting Antibody-Drug Conjugate SYD985. Mol. Pharm. 12, 1813–1835. 10.1021/mp500781a. [PubMed: 25635711]
43. BioSpace (2021). Byondis announces positive topline results of pivotal phase III TULIP® study in patientswith HER2-positive unresectable locally advanced or metastatic breast cancer. News release. Byondis B.V June 8, 2021. https://www.biospace.com/article/releases/byondis-announces-positive-topline-results-of-pivotal-phase-iii-tulip-study-in-patients-with-her2-positive-unresectable-locally-advanced-or-metastatic-breast-cancer/.
44. Dal Corso A, Pignataro L, Belvisi L, and Gennari C (2019). Innovative Linker Strategies for Tumor-Targeted Drug Conjugates. Chem. Eur. J 25, 14740–14757. 10.1002/chem.201903127. [PubMed: 31418970]
45. Kisin-Finfer E, Ferber S, Blau R, Satchi-Fainaro R, and Shabat D (2014). Synthesis and evaluation of new NIR-fluorescent probes for cathepsin B: ICT versus FRET as a turn-ON mode-of-action. Bioorg. Med. Chem. Lett. 24, 2453–2458. 10.1016/j.bmcl.2014.04.022. [PubMed: 24767838]
46. Dal Corso A, Borlandelli V, Corno C, Perego P, Belvisi L, Pignataro L, and Gennari C (2020). Fast Cyclization of a Proline-Derived Self-Immolative Spacer Improves the Efficacy of Carbamate Prodrugs. Angew. Chem. Int. Ed 59, 4176–4181. 10.1002/anie.201916394.
47. Xu S, Liu H-W, Chen L, Yuan J, Liu Y, Teng L, Huan S-Y, Yuan L, Zhang X-B, and Tan W (2020). Learning from Artemisinin: Bioinspired Design of a Reaction-Based Fluorescent Probe for the Selective Sensing of Labile Heme in Complex Biosystems. J. Am. Chem. Soc. 142, 2129–2133. 10.1021/jacs.9b11245. [PubMed: 31955575]
48. Chen C, and Paw BH (2012). Cellular and mitochondrial iron homeostasis in vertebrates. Biochim. Biophys. Acta 1823, 1459–1467. 10.1016/j.bbamcr.2012.01.003. [PubMed: 22285816]
49. Ganz T, and Nemeth E (2012). Hepcidin and iron homeostasis. Biochim. Biophys. Acta 1823, 1434–1443. 10.1016/j.bbamcr.2012.01.014. [PubMed: 22306005]
50. Liu F, Song Y, and Liu D (1999). Hydrodynamics-based transfection in animals by systemic administration of plasmid DNA. Gene Ther. 6, 1258–1266. 10.1038/sj.gt.3300947. [PubMed: 10455434]
51. Kamimura K, Yokoo T, Abe H, Kobayashi Y, Ogawa K, Shinagawa Y, Inoue R, and Terai S (2015). Image-Guided Hydrodynamic Gene Delivery: Current Status and Future Directions. Pharmaceutics 7, 213–223. 10.3390/pharmaceutics7030213. [PubMed: 26308044]
52. Sherf B, Navarro S, Hannah R, and Wood K (1996). Dual-LuciferaseTM Reporter Assay: An Advanced Co-Reporter Technology Integrating Firefly and Renilla Luciferase Assays. Promega Notes Magazine 57.
53. Bhaumik S, and Gambhir SS (2002). Optical imaging of Renilla luciferase reporter gene expression in living mice. Proc Natl Acad Sci USA 99, 377–382. 10.1073/pnas.012611099. [PubMed: 11752410]

54. Preza GC, Ruchala P, Pinon R, Ramos E, Qiao B, Peralta MA, Sharma S, Waring A, Ganz T, and Nemeth E (2011). Minihepcidins are rationally designed small peptides that mimic hepcidin activity in mice and may be useful for the treatment of iron overload. J. Clin. Invest. 121, 4880–4888. 10.1172/JCI57693. [PubMed: 22045566]
55. Menna P, Paz OG, Chello M, Covino E, Salvatorelli E, and Minotti G (2012). Anthracycline cardiotoxicity. Expert Opin. Drug Saf. 11 Suppl 1, S21–36. 10.1517/14740338.2011.589834. [PubMed: 21635149]
56. Poli G, Biasi F, and Leonarduzzi G (2008). 4-Hydroxynonenal-protein adducts: A reliable biomarker of lipid oxidation in liver diseases. Mol. Aspects Med. 29, 67–71. 10.1016/j.mam.2007.09.016. [PubMed: 18158180]
57. Protchenko O, Baratz E, Jadhav S, Li F, Shakoury-Elizeh M, Gavrilova O, Ghosh MC, Cox JE, Maschek JA, Tyurin VA, et al. (2021). Iron chaperone poly rc binding protein 1 protects mouse liver from lipid peroxidation and steatosis. Hepatology 73, 1176–1193. 10.1002/hep.31328. [PubMed: 32438524]
58. Chen J, Li X, Ge C, Min J, and Wang F (2022). The multifaceted role of ferroptosis in liver disease. Cell Death Differ. 29, 467–480. 10.1038/s41418-022-00941-0. [PubMed: 35075250]
59. Jiang H, Muir RK, Gonciarz RL, Olshen AB, Yeh I, Hann BC, Zhao N, Wang Y-H, Behr SC, Korkola JE, et al. (2022). Ferrous iron-activatable drug conjugate achieves potent MAPK blockade in KRAS-driven tumors. J. Exp. Med. 219. 10.1084/jem.20210739.
60. Ghoochani A, Hsu E-C, Aslan M, Rice MA, Nguyen HM, Brooks JD, Corey E, Paulmurugan R, and Stoyanova T (2021). Ferroptosis inducers are a novel therapeutic approach for advanced prostate cancer. Cancer Res. 81, 1583–1594. 10.1158/0008-5472.CAN-20-3477. [PubMed: 33483372]
61. Chen Y-C, Oses-Prieto JA, Pope LE, Burlingame AL, Dixon SJ, and Renslo AR (2020). Reactivity-Based Probe of the Iron(II)-Dependent Interactome Identifies New Cellular Modulators of Ferroptosis. J. Am. Chem. Soc. 142, 19085–19093. 10.1021/jacs.0c06709. [PubMed: 33124817]
62. Cai LL, Ruberto RA, Ryan MJ, Eaton JK, Schreiber SL, and Viswanathan VS (2020). Modulation of ferroptosis sensitivity by TXNRD1 in pancreatic cancer cells. BioRxiv. 10.1101/2020.06.25.165647.
63. Tousignant KD, Rockstroh A, Poad BLJ, Talebi A, Young RSE, Taherian Fard A, Gupta R, Zang T, Wang C, Lehman ML, et al. (2020). Therapy-induced lipid uptake and remodeling underpin ferroptosis hypersensitivity in prostate cancer. Cancer Metab. 8, 11. 10.1186/s40170-020-00217-6. [PubMed: 32577235]
64. Chen G-Q, Benthani FA, Wu J, Liang D, Bian Z-X, and Jiang X (2020). Artemisinin compounds sensitize cancer cells to ferroptosis by regulating iron homeostasis. Cell Death Differ. 27, 242–254. 10.1038/s41418-019-0352-3. [PubMed: 31114026]
65. Eling N, Reuter L, Hazin J, Hamacher-Brady A, and Brady NR (2015). Identification of artesunate as a specific activator of ferroptosis in pancreatic cancer cells. Oncoscience 2, 517–532. 10.18632/oncoscience.160. [PubMed: 26097885]
66. Abrams RP, Carroll WL, and Woerpel KA (2016). Five-Membered Ring Peroxide Selectively Initiates Ferroptosis in Cancer Cells. ACS Chem. Biol. 11, 1305–1312. 10.1021/acschembio.5b00900. [PubMed: 26797166]
67. Gonciarz RL, Collisson EA, and Renslo AR (2021). Ferrous Iron-Dependent Pharmacology. Trends Pharmacol. Sci. 42, 7–18. 10.1016/j.tips.2020.11.003. [PubMed: 33261861]
68. Spangler B, Fontaine SD, Shi Y, Sambucetti L, Mattis AN, Hann B, Wells JA, and Renslo AR (2016). A Novel Tumor-Activated Prodrug Strategy Targeting Ferrous Iron Is Effective in Multiple Preclinical Cancer Models. J. Med. Chem. 59, 11161–11170. 10.1021/acs.jmedchem.6b01470. [PubMed: 27936709]
69. Gonciarz RL, Sakhamuri S, Hooshdaran N, Kumar G, Kim H, Evans MJ, and Renslo AR (2023). Elevated labile iron in castration-resistant prostate cancer is targetable with ferrous iron-activatable antiandrogen therapy. Eur. J. Med. Chem. 249, 115110. 10.1016/j.ejmech.2023.115110. [PubMed: 36708680]

70. Varghese F, Bukhari AB, Malhotra R, and De A (2014). IHC Profiler: an open source plugin for the quantitative evaluation and automated scoring of immunohistochemistry images of human tissue samples. PLoS ONE 9, e96801. 10.1371/journal.pone.0096801. [PubMed: 24802416]

71. Schneider CA, Rasband WS, and Eliceiri KW (2012). NIH Image to ImageJ: 25 years of image analysis. Nat. Methods 9, 671–675. 10.1038/nmeth.2089. [PubMed: 22930834]

72. Blank BR, Gonciarz RL, Talukder P, Gut J, Legac J, Rosenthal PJ, and Renslo AR (2020). Antimalarial Trioxolanes with Superior Drug-Like Properties and In Vivo Efficacy. ACS Infect. Dis. 6, 1827–1835. 10.1021/acsinfecdis.0c00064. [PubMed: 32369341]

Highlights:

- FeAL-1 releases D-luciferin upon sensing labile ferrous iron in cells or animals.
- FeAL-1 shows enhanced sensitivity compared to first-generation probe ICL-1.
- FeAL-1 detected changes in labile iron levels in mouse livers and xenografts.

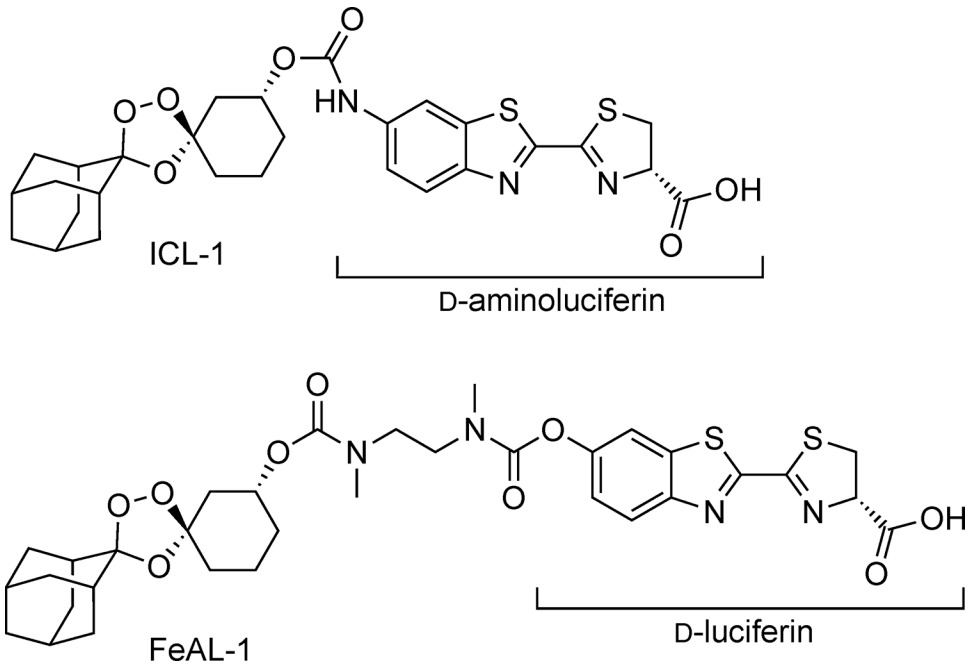

Figure 1. Structures of ICL-1 and FeAL-1.

Structures of first-generation *in vivo* labile iron probe ICL-1 and new probe FeAL-1 described herein. FeAL-1 is conjugated to phenolic D-luciferin via an extended linker.

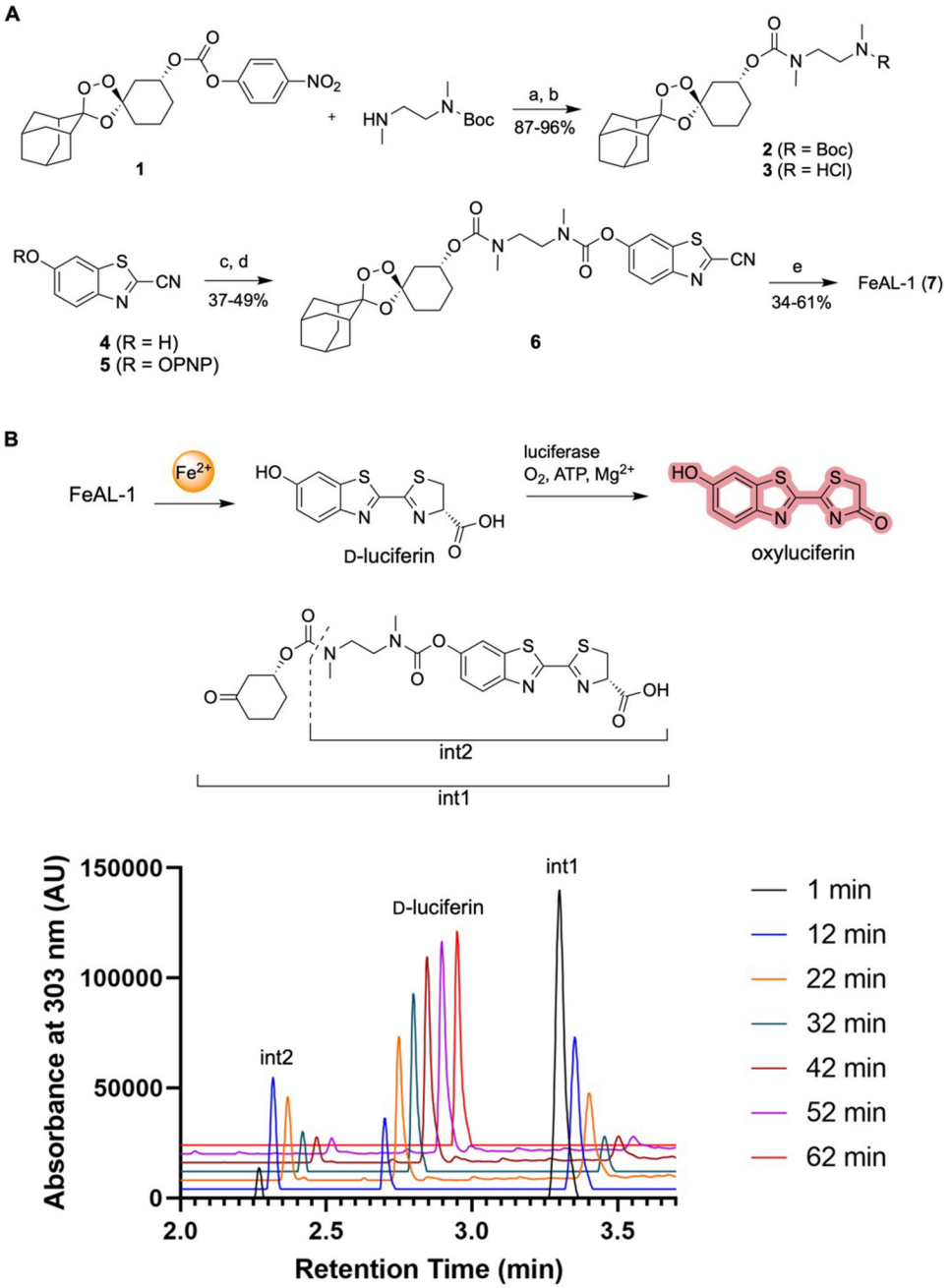

Figure 2. Synthesis and activation studies of FeAL-1.

Synthesis of FeAL-1 and its hemin-promoted activation to release D-luciferin. (**A**) Optimized synthesis of FeAL-1 starting from the enantiopure trioxolane intermediate (*R,R*)-**1**. Conditions: (a) Et_3N, CH_2Cl_2, rt, 2h; (b) AcCl, MeOH, 0 °C to rt, 12 h; (c) (4-NO_2Ph)OC(O)Cl, Et_3N, THF, 0 °C, 2.5 h; (d) intermediate **3**, 0 °C, 1 h; (e) D-cysteine•H_2O, CH_2Cl_2/MeOH/H_2O (3:3:1), K_2CO_3, 1h. (**B**) Stacked UPLC chromatograms across a 62 min time course confirm the release of D-luciferin via int1 and int2 in reaction media containing ferrous hemin. FeAL-1 has been completely consumed by the 1-minute time point while released D-luciferin is detected by the second time point at 12 minutes.

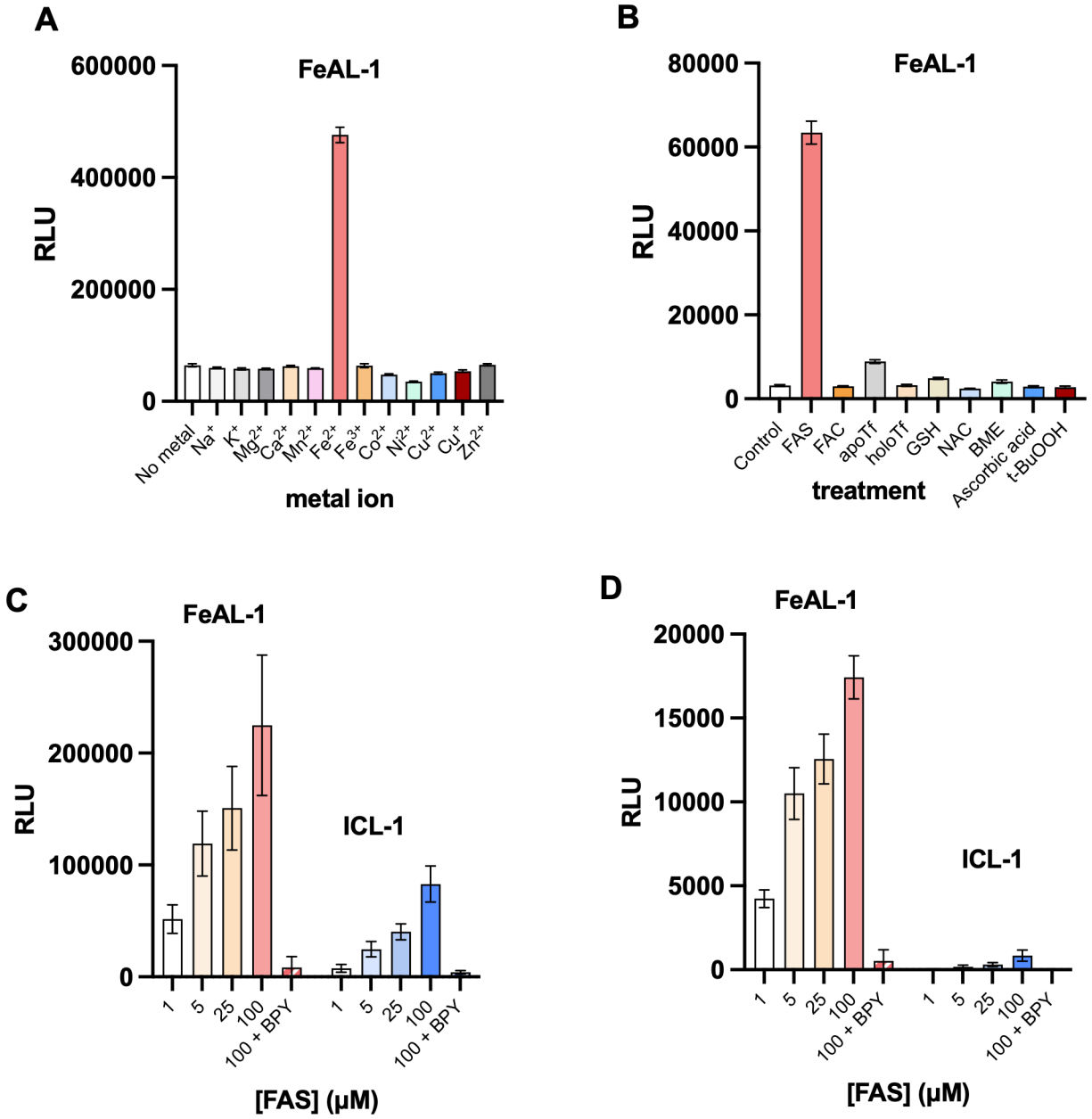

Figure 3. Selectivity of FeAL-1 activation under cell-free conditions.

Cell-free luminescent response of 2.5 μM FeAL-1 imaged 5 minutes after the addition of luciferase (10 μg/mL) and after 2 hours pre-treatment with (**A**) Biologically relevant s-block (1 mM) and d-block (100 μM) metal ions, or 30 minutes pre-treatment with (**B**) Transferrin protein (apoTf and holoTf at 100 μM), or 1 mM glutathione (GSH), *N*-acetyl cysteine (NAC), β-mercaptoethanol (BME), ascorbic acid, or *tert*-butyl hydroperoxide (t-BuOOH). Positive and negative controls ferrous ammonium sulfate (FAS, 100 μM) and ferric ammonium citrate (FAC, 1 mM). Panels **C** and **D**: cell-free luminescent response of 5 μM FeAL-1 (red bars) or 5 μM ICL-1 (blue bars) in the presence of 100 μg/mL luciferase, following a 90 min incubation of each probe with indicated concentrations of FAS, with

or without 250 μM iron-chelator 2,2-bipyridine (BPY). Data from (**C**) is for imaging at 1 minute and panel (**D**) at 6 minutes after the addition of luciferase.

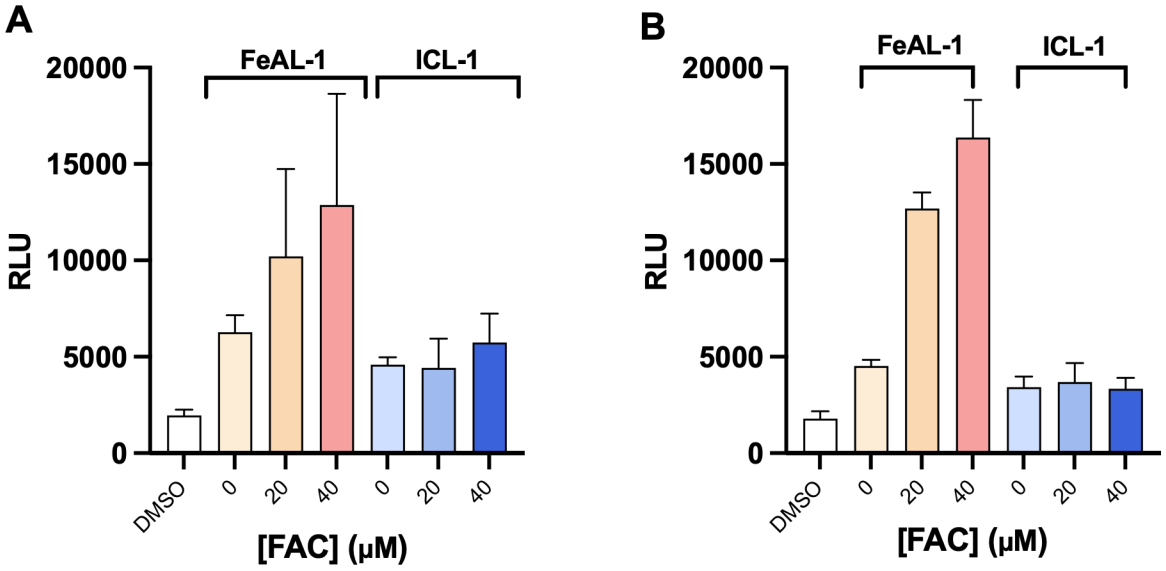

Figure 4. Comparing cellular responses of ICL-1 and FeAL-1.

Comparison of the cellular response of 20 μM FeAL-1 (red bars) and 20 μM ICL-1 (blue bars) in luciferase expressing MiaPaca2-luc (**A**) and SW1990-luc (**B**) cells pretreated with the indicated concentrations of ferric ammonium citrate (FAC) for 2 hours prior to addition of probe and imaging after another 15 minutes.

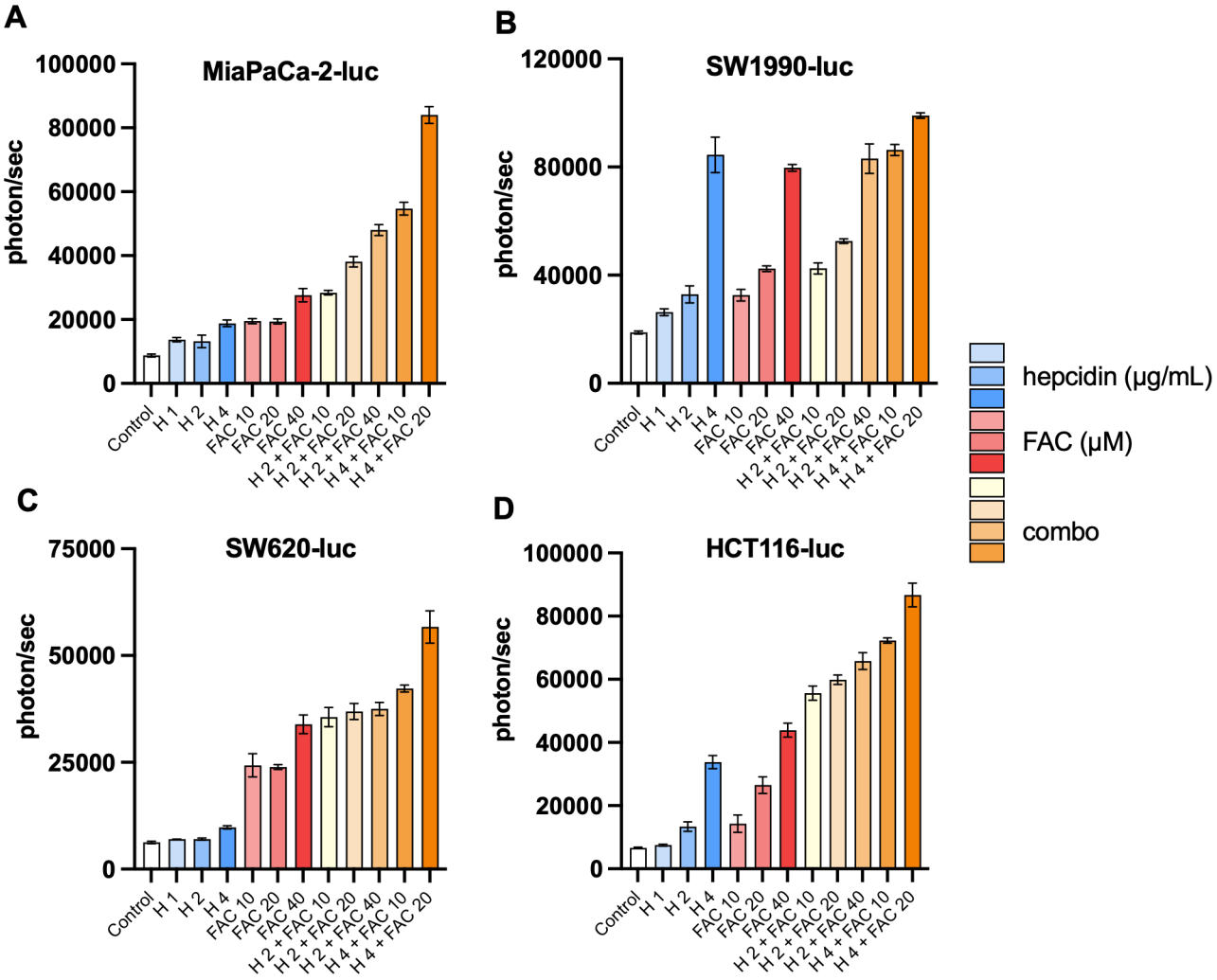

Figure 5. Bioluminescent response of FeAL-1 to modulation of labile iron levels in cells.

Bioluminescent signal following incubation of FeAL-1 with luciferase-expressing cancer cell lines pre-treated with varying concentrations of hepcidin (H, in µg/mL), ferric ammonium citrate (FAC, in µM), or combinations thereof. Cells were supplemented with FAC for 2 hours prior to the addition of FeAL-1 (75 µM) followed by an additional 30 min incubation before imaging. For hepcidin treatments, cells were pretreated with hepcidin (H) (1–4 µg/mL) for 16 hours which was sustained during FAC treatment. Luciferase-expressing cell lines are: (**A**) MiaPaCa-2-luc (**B**) SW1990-luc (**C**) SW620-luc and (**D**) HCT116-luc. Error bars are ±SD (n = 3).

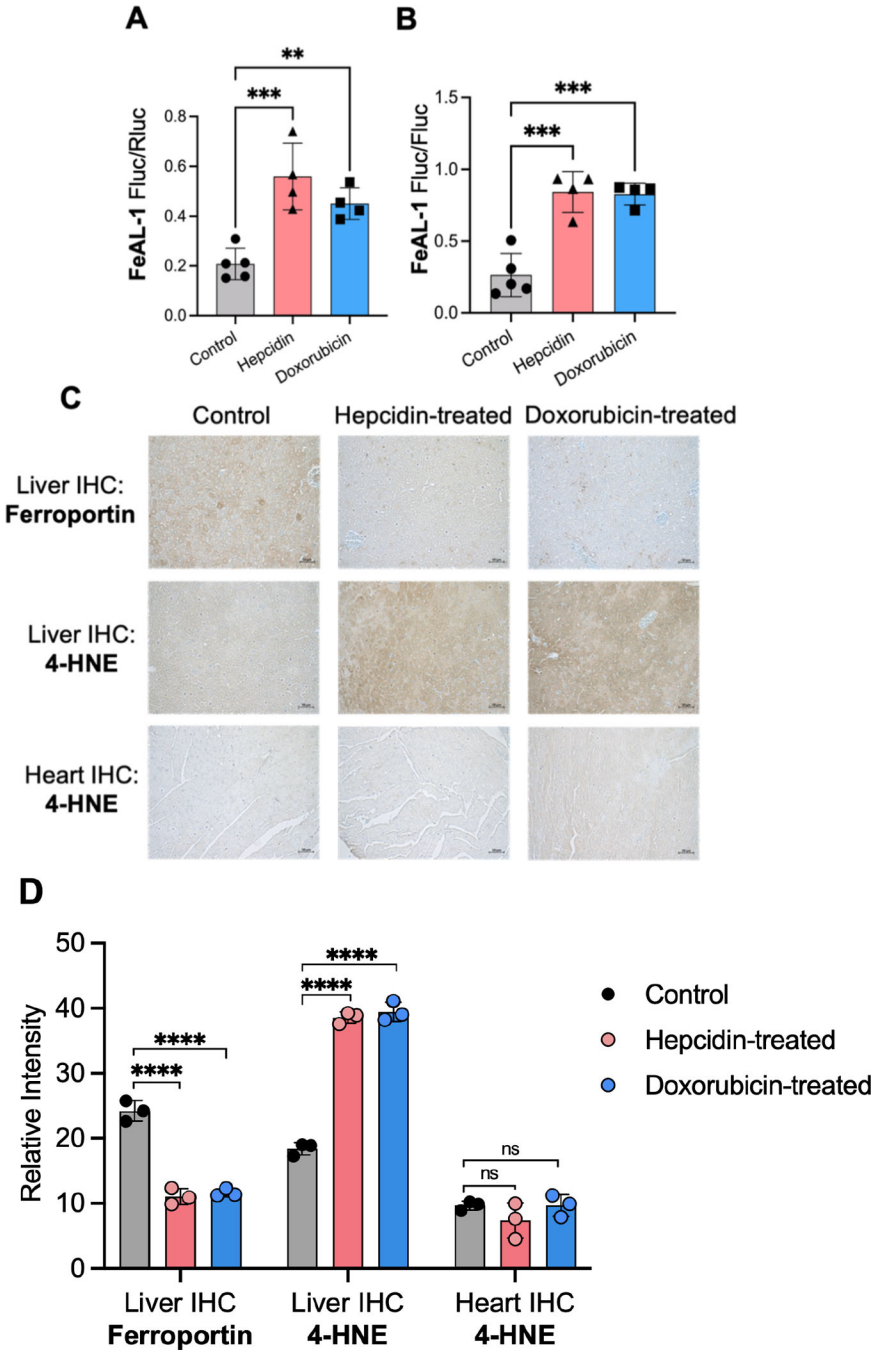

Figure 6. FeAL-1 detects changes in labile iron levels in the livers of mice.

Imaging mouse liver with FeAL-1 in a dual-reporter (Fluc/Rluc) system reveals elevated LIP in mice pre-treated with hepcidin or doxorubicin compared to untreated controls. (**A**) Bioluminescent signal 25 min after administration of FeAL-1 (36 mg/kg, IP) in the untreated control group (grey), a group pre-treated with hepcidin (red, 50 μg/mouse/day hepcidin for three days prior to imaging) or a DOX-treated group (blue, 10 mg/kg, single dose administrated five days prior to imaging). Bioluminescent signal of FeAL-1 is normalized to that measured after coelenterazine treatment in the same animals (FeAL-1 Fluc/Rluc).

(**B**) FeAL-1 bioluminescent signal normalized to that obtained after D-luciferin treatment in the same animals (FeAL-1 Fluc/Fluc).(**C**) Representative liver and heart tissue slices stained with anti-ferroportin or 4-hydroxynonenal (4-HNE) antibodies in control, and hepcidin-, or DOX-treated mice. (**D**) Quantification of staining liver and heart tissue slices treated with anti-ferroportin (FPN) or anti-4-hydroxynonenal (4-HNE) antibodies in control, and hepcidin-, or DOX-treated mice (n=3 per condition; the full set of images analyzed are provided in Figure S10). Statistical analyses for A and B were performed with one-way ANOVA with multiple comparisons to the control group (**, $P \leq 0.01$ and ***, $P \leq 0.001$). Statistical analyses for D were performed with two-way ANOVA with multiple comparisons to the control group (ns, $P > 0.05$ and ****, $P \leq 0.0001$).

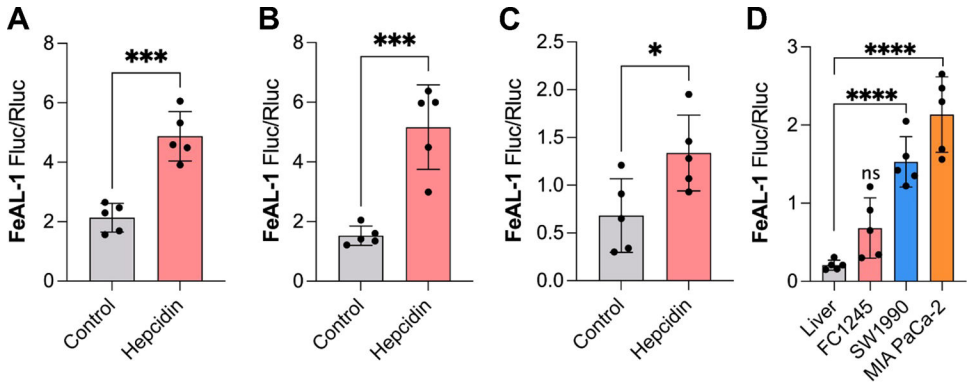

Figure 7. FeAL-1 detects changes in labile iron levels in mouse xenograft models.

Imaging LIP with FeAL-1 in dual-reporter mouse PDA models. (**A**) Bioluminescent signal after administration of FeAL-1 (36 mg/kg, IP) in the orthotopically implanted MIA PaCa-2 dual reporter (Fluc/Rluc) tumor model. Untreated control (grey) and hepcidin treated groups (red, 50 μg/mouse for three days prior to imaging) are shown. Bioluminescent output from FeAL-1 is normalized to that arising from coelenterazine treatment in the same animals (FeAL-1 Fluc/Rluc). (**B**) Treatments and protocol as described in **A** but using an orthotopically implanted (Fluc/Rluc) SW1990 tumor model. (**C**) Treatments and protocol as described in **A** but using an orthotopically implanted (Fluc/Rluc) FC1245 tumor model. (**D**) Comparison of normalized FeAL-1 response between control groups of dual-reporter (Fluc/Rluc) mouse liver and mouse PDA models (FC1245, SW1990 and MIA PaCa-2 tumor models). Statistical analyses were performed by two-tailed t-test for panels A-C (*, $P \leq 0.05$ and ***, $P \leq 0.001$) and for panel D with one-way ANOVA with multiple comparisons to the control group (ns, $P > 0.05$ and ****, $P \leq 0.0001$).

Key Resources Table

REAGENT OR RESOURCE	SOURCE	IDENTFIER
Antibodies		
Anti-Ferroportin/SLC40A1 Antibody	Novus Bio	Cat#NBP1–21502
Chemicals, peptides, and recombinant proteins		
For cell-free assays: Luciferase from Photinus pyralis (firefly), recombinant, expressed in *E. coli*, lyophilized powder, ≥10×10^{10} units/mg protein	Sigma-Aldrich	Cat#SRE0045; CAS: 61970-00-1
XenoLight D-Luciferin potassium salt	PerkinElmer	Cat#12799
D-luciferin free acid	Gold Biotechnology	Cat#L-123
ATP (100 mM solution)	Thermo Scientific	Cat#FERR0441
Hepcidin-25 trifluoroacetate	VWR	Cat# H-5926.1000BA
Ammonium iron(II) sulfate hexa-hydrate (99%) (FAS)	Sigma-Aldrich	Cat# 215406; CAS: 7783-85-9
Ferric ammonium citrate (FAC)	Spectrum	Cat# F1000; CAS: 1185-57-5
Calcium chloride (≥97%)	Sigma-Aldrich	Cat# C4901; CAS: 10043-52-4
Nickel(II) chloride (98%)	Sigma-Aldrich	Cat# 339350; CAS: 7718-54-9
Magnesium chloride (≥99%)	Sigma-Aldrich	Cat# M8266; CAS: 7786-30-3
Copper(II) chloride (97%)	Sigma-Aldrich	Cat# 222011; CAS: 7447-39-4
Iron(II) chloride (98%)	Sigma-Aldrich	Cat# 372870 CAS: 7758-94-3
Cobalt (II) chloride (97%)	Sigma-Aldrich	Cat# 232696 CAS: 7646-79-9
Zinc chloride (≥98%)	Sigma-Aldrich	Cat# 208086; CAS: 7646-85-7
Manganese(II) chloride (≥99%)	Sigma-Aldrich	Cat# M1787; CAS: 7773-01-5
Tetrakis(acetonitrile)copper(I) hexafluorophosphate (97%)	Sigma-Aldrich	Cat# 346276; CAS: 64443-05-6
2,2’-Bipyridine (97%)	Combi-blocks	Cat# OR-2343; CAS: 366-18-7
Recombinant DNA		
pCMV-IRES-Renilla Luciferase-IRES-Gateway-Firefly Luciferase (pIRIGF)	Addgene	Addgene#101139
Software and algorithms		
GraphPad Prism 9	GraphPad	https://graphpad.com
ChemDraw Professional 22.0	PerkinElmer	https://perkinelmer.com
ImageJ	NIH[71]	https://imagej.nih.gov/ij/